# Background and specific contrast enhancements for imaging biological samples with micro-computational tomography

Master's Thesis

Ilmari Tamminen

BioMediTech

University of Tampere

07.05.2014

# Acknowledgements

Finally, even though a scientist needs to satisfy his thirst of curiosity, as human beings we also need personal support and friends outside from the scientific institutions. That is why I want to thank my girlfriend, Mari Vanhatalo, who have patiently let this quick and vivid minded writer to do and participate in many personal and formal projects also outside of this thesis. I would also like to thank my close parents and uncle, who have taught me to be alert, analytical, thorough and view the world as comprehensively and objectively as possibly. They also gave me their will to advance in life, no matter how tough it might sometimes feel. I would also like to thank my funny friends who have shared many enjoyable moments with me, at the same time giving their honest aspects during many thoughtful and interesting conversations.

Many thanks to you all!

07.05.2014

Ilmari Tamminen

# Pro gradu –tutkielma

# Tiivistelmä

**Tutkielman tausta ja tavoitteet:** Tyypillisesti röntgenkuva muodostuu näytteen aiheuttaman säteen attenuaation avulla. Biologisissa näytteissä ja biomateriaaleissa yleinen ongelma on niiden pieni tiheys ja sen tasainen jakauma. Ilman raskaiden alkuaineiden kuljettamista näytteisiin, ei tutkittavia piirteitä saada mikro-tomografiakuvantamisella (µCT) erotettua lainkaan, tai kuvan muodostaminen vaatii liikaa aikaresursseja. Tämän tutkimuksen tarkoituksena oli koestaa ja optimoida erilasia tausta- sekä spesifejä kontrastointimenetelmiä edellä mainittujen haasteiden ratkaisemiseksi.

**Materiaalit ja menetelmät:** Taustakontrastointimenetelmistä kokeiltiin jodiin ja fosfovolframihappoon perustuvia varjoaineita. Kontrastointimenetelmiä optimoitiin iteroimalla niin kauan, että kullakin varjoaineella saatiin aikaan tyydyttäviä tuloksia tutkittaessa aikuisten seeprakalojen kolmiulotteista anatomiaa. Etanolipohjaista jodikontrastointia käytettiin myös terveiden ja dystrofisten rotan silmien morfologisten erojen tutkimiseksi. Yksisolukerroksisia kantasolunäytteitä käsiteltiin spesifein värjäyksin, joissa vasta-aineita hyödyntämällä metallista hopeaa lokalisoitiin kulloinkin kohteena olevan antigeenin välittömään läheisyyteen.

**Tulokset:** Kaikki kokeillut kontrastointimenetelmät korostivat tutkittavia piirteitä µCT-kuvatuissa näytteissä. Kaikki epäspesifit kontrastointimenetelmät toivat selkeästi ja monipuolisesti esiin aikuisten seeprakalojen anatomiaa. Lisäksi etanolipohjainen jodiointi säilytti rotan silmien yleisen morfologian, samalla kun retinoita tarkastelemalla pystyttiin osoittamaan selviä hienorakenteellisia eroja terveiden ja dystrofisten silmien välillä. Spesifit kontrastointimenetelmät korostivat onnistuneesti yksisolukerrosolosuhteissa aktiini- ja lamiiniproteiiniesiintymiä tutkituissa kantasoluissa.

**Johtopäätökset:** Kokeillut kontrastointimenetelmät antavat hyvän ja kattavan pohjan moninaisille jatkotutkimuksille kuvattaessa mitä erilaisempia biologisia näytteitä µCT-laitteistolla.

**Avainsanat:** µCT, varjoaine, taustakontrastointi, vasta-aineet, histologiset näytteet, kantasolut

# Master's thesis

Place:        University of Tampere, BioMediTech
Author:       Tamminen, Ilmari Veikko Hjalmar
Title:        Background and specific contrast enhancements for imaging biological samples with micro-computational tomography
Pages:        62 s.
Supervisors:  Professor Jari Hyttinen, PhD Antti Aula
Reviewed:     Professors Jari Hyttinen and Markku Kulomaa
Date:         May 2014

# Abstract

**Background and aims:** Typically, an X-ray image forms as the applied ray becomes attenuated by the imaged sample. In biological and biomaterial samples, the common imaging issue is the low density and its homogeneous distribution. Without externally supplied heavy elements, studied features may not be visible at all, or the micro-computational tomography ($\mu$CT) imaging may take unreasonable amount of time resources. The goal of this study was to test and optimize different background and specific contrast enhancement methods for overcoming these imaging issues.

**Materials and methods:** The used background contrasting methods were based on iodine and phosphotungstic acid. Each staining method were iterated until satisfactory contrasting results were gained for examining the three dimensional anatomy of adult zebra fish. The ethanol based iodine was also used for studying the structural dissimilarities between dystrophic and healthy rat retinas. Stem cell monolayer samples were specifically stained by antibodies which were used for localizing metallic silver in the immediate proximity of the examined antigens.

**Results:** During the research it was shown that all of the used contrasting methods were capable for enhancing the studied features in the treated samples. All of the background contrasting methods successfully enhanced the anatomical features of the adult zebra fish. Furthermore, the ethanol based iodine contrasting preserved the general morphology of the rat eyes and made possible for distinguishing clear structural dissimilarities between dystrophic and control retinas. The specific contrasting method enhanced successfully the target actin and lamin antigens in the examined stem cell monolayer samples.

**Conclusions:** The used contrasting methods gave good and comprehensive base for the following research for examining wide variety of biological samples with $\mu$CT.

**Keywords:** $\mu$CT, contrasting agent, background contrasting, antibodies, histological samples, stem cells

# Table of content

# Abbreviations

| | |
|---|---|
| µCT | Micro-computational tomography |
| ASC | Adipose stem cell |
| BSA | Bovine serum albumin |
| *c* | The speed of light |
| CCD | Charge-coupled device |
| CD | Cluster of differentiation |
| CT | Computational tomography |
| DAPI | 4',6-diamidino-2-phenylindole |
| E | Energy |
| EMC | Extracellular matrix |
| eV | Electron volts |
| *f* | Frequency |
| FOV | Field of view |
| GAG | Glycosaminoglycan |
| *h* | Planck constant |
| HE | Hematoxylin and eosin |
| HRP | Horseradish peroxidase |
| I | Current or intensity |
| I2E | Solution of elemental iodine dissolved in absolute ethanol |
| IKI | Iodine and potassium iodide (Lugol's solution) |
| P | Power |
| PBS | Phosphate buffered saline |
| PTA | Phospho tungstic acid |
| RCS | Royal College Surgeons |
| RPE | Retinal pigment epithelium |
| RT | Room temperature |
| SNR | Signal to noise ratio |
| TBS | Tris buffered saline |
| V | Voltage |
| w/v | Weight to volume |
| λ | Wavelength |

# 1. Introduction

X-ray computed tomography (CT) is a widely used imaging method in medicine. CT imaging differs from the conventional X-ray radiographs by its capability to produce 3D *in silico* visualizations from the target. The target is imaged from multiple different angles by rotating either the source-detector apparatus, i.e. gantry, or the target itself, and the imaging data is processed by a so called backprojection algorithm for making the reconstruction. The contrast of the transillumination images, or projections, arise from the varying content of the sample and, or more precisely, from the varying electron densities. For example, by illuminating electron dense tissues, like bone, with a constant X-ray luminosity, the intensity behind the sample is smaller than after illuminating softer areas, like muscles. (Webb, 1988) That is because the target with the higher effective atomic number absorbs and scatters incident X-ray photons more likely and, thus, attenuates the X-ray intensity seen by the detector (Seibert & Boone, 2005).

3D pixel matrices, the virtual reconstructions made from the samples, are orthodoxically called voxel matrices. CT machines capable to produce high spatial resolution data, in the order of micrometers, are referred to X-ray microtomography (μCT) devices. Depending on the used hardware, the voxel size can go down to micrometer scale (Ritman, 2002; Metscher, 2009; Hainfeld et al., 2011; Zehbe et al., 2010; Eck et al., 2010; Metscher & Muller, 2011; Thimm et al., 2012), even down to submicron resolutions if specific equipment are available (Brunkea et al., 2008). Because of the high resolution capabilities and the possibility to image samples in their native 3D states, μCT devices can be used for biomedical research. For example, one can use μCT technology for studying the intravascular distributions of endothelial antigens in small mammals (Eck et al., 2010), gene product distributions in the tissues of embryos (Metscher & Muller, 2011) or cell adhesion and proliferation in biomaterials (Dorsey et al., 2009; Zehbe et al., 2010; Thimm et al., 2012; Watlinga et al., 2010). Furthermore, by the possibility to skip the many steps of the conventional histology, just by staining whole samples and then imaging them, μCT technology offers an economical and fast way to do histological research. This is specifically true in pure morphological studies where simple, non-specific background contrasting is sufficient for making the studied features visible. Because of the penetrativity of the X-ray photons, even internal parts of thick, opaque samples can be examined by μCT devices. (Metscher, 2009)

Commonly, the electron density variation in soft material samples is too low for acquiring good X-ray contrast. The easiest way to enhance the general X-ray contrast is to use so called in-line phase contrasting and/or transport heavy elements, in other words contrast agents or stains, into the sample. Usually, µCT setups using synchrotron sources are capable of generating X-ray images with good phase contrasting and can be used for studying unstained soft material samples (see *X-ray sources* and *In-line phase contrast imaging* for more information). However, sometimes contrast agents are the only way for making studied features visible (see *Non-specific and specific contrasting*). The easiest way to enhance the attenuation contrast is to simply immerse the samples in background contrasting solution. Because of the initial chemical unbalance, staining molecules start to diffuse into the sample. The stabilization continues until a new chemical balance is reached and the net flow of molecules in and out of the sample is zero. The distribution of contrasting agents depends on the content of the sample and the chemical nature of the staining substances (see *Non-specific and specific contrasting* for more information). After staining, higher signal intensity, meaning lower X-ray intensity coming through the sample, can be seen where the contrast agents are localized. For examining only specific structures, antibodies and other specifically binding molecules can be applied for localizing the contrasting elements by specific manner. These target recognizing molecules can be conjugated to enzymes for example, which can be further used for producing local metal precipitates (Metscher & Muller, 2011; Chien et al., 2013). Dual complementarity, without any enzyme activity, may also be used for linking initially dense substances directly with the studied target structures (Thimm et al., 2012).

Like stated above, µCT imaging can be applied for examining general 3D features of a sample and for distinguishing highly specific molecular details and their spatial distributions. In the following literature review, the main technical and physical details of µCT technology and different contrasting methods are discussed more carefully. The aim of the practical part of this thesis was to test and advance the contrast enhanced µCT imaging based on X-ray tube radiation. The feasibilities of common background contrasting methods are tested and optimized for examining different kinds of histological samples. Earlier work shows how three common background contrasting agents can be applied on relatively small histological samples, like on chick embryos (Metscher, 2009), but does not provide data about how they suit on bigger samples, like adult zebra fish. Moreover, the discussion about the reliability of the phosphotungstic acid (PTA) contrasting, its possible precipitation with endogenous phosphates etc., seems to be somewhat incomplete

(Metscher, 2009). Even the PTA distribution itself in bigger samples is an uncompleted issue in some articles (Pauwels et al., 2013). In this thesis, the work is finished, as the PTA stain, based on strong negative charges and their interactions in a sample, is a good additional stain in the µCT contrasting toolbox in addition to iodine. Iodine based stain is further applied on rat eyes for showing the very first time how the contrast enhanced µCT imaging can be used for examining the fine structural dissimilarities between the eyes suffering dystrophy and healthy ones. Finally, specific antibody contrasting is tested and optimized parallel with the conventional labeling methods for examining antigen distributions and the labeling reliability in cultured cells. Antibody technologies are already applied on cell-biomaterial hybrid samples (Thimm et al., 2012), even subcellular structures are claimed to be resolved by µCT imaging (Chien et al., 2013), but it seems that no high resolution µCT data is available, acquired by using X-ray tube radiation instead of extremely sophisticated synchrotron sources.

# 2. Review of the literature

## 2.1. Technology and physics behind the µCT imaging

In the coming sub-sections, the main technical features and physics behind the µCT imaging are discussed. Before going any further into the physics of the X-ray imaging, it is good to remember how energy (E), frequency ($f$) and wavelength (λ) of photons are related to each other. The terms can be related to each other by the simple formula:

$$E_{photon} = hc/\lambda = hf \qquad [1]$$

where $h$ is the Planck constant and $c$ the speed of light. Thus, when describing the features of photons, there are three fundamental proportionalities to remember:

$$E_{photon} \propto f \qquad [2]$$
$$E_{photon} \propto 1/\lambda \qquad [3]$$
$$\lambda \propto 1/f \qquad [4]$$

### 2.1.1. X-ray sources

In µCT devices, X-rays are produced either by X-ray tube sources (Metscher, 2009; Hainfeld et al., 2011; Eck et al., 2010; Metscher & Muller, 2011; Jeffery et al., 2011; Cox and Jeffery, 2011; Holdsworth & Thornton, 2002) or by synchrotron sources (Thimm et al., 2012; Yue et al., 2010; Zehbe et al., 2010). X-ray tube sources are cheaper, smaller and simpler in structure, but cannot produce the best possible image quality because the radiation they emit is polychromatic and non-coherent (see *Imaging parameters and related physics* for more information). Instead, synchrotron sources are expensive, enormous facilities, capable of producing extremely coherent and monochromatic high intensity X-ray radiation (Görlich, 2009). (Brunkea et al., 2008)

Basically, the X-ray tube sources are electrically polarized vacuum tubes (figure 1). The cathode, which is a thin metal filament, is heated by heating current and relatively low voltage. Electrons, emitted by the heat, are pulled towards the anodic end of the X-ray tube by high acceleration voltage ($V_{acceleration}$). (Daneke & Schanklies, 2004) The range of available photon energies is much wider with the synchrotron sources, but generally, energies from 1 keV to hundreds of keV can be used. The energy spectrum of tube sources fits inside of this larger range and space is left between the extreme ends of each type of radiation. (Brunkea et al., 2008; Görlich, 2009) In the μCT tube sources, the electron beam is regulated and guided by specific magnetic stages for producing a small focal spot (Schambach et al., 2010; Daneke & Schanklies, 2004). The focal spot is focused into a so called transmission target, which is usually made of tungsten, molybdenum or copper. These metals have high atomic numbers, why the accelerated electrons likely interact with the target atoms and are slowed down. When an electron decelerates, its kinetic energy ($E_{kinetic}$) is released as a photon ($E_{photon}$). The released $E_{photon}$ cannot be bigger than the lost $E_{kinetic}$. In tube radiation, only a few photons have energies close to this maximum, as the $E_{kinetic}$ is usually released during multiple collisions with the target atoms, why the spectrums of lower photon energies are produced. The produced X-ray photons are emitted somewhat in parallel with the emitted electrons and the X-ray beam spreads out from the anodic end of the tube. (Daneke & Schanklies, 2004)

X-ray tube sources can be further divided into two groups depending on their performance. If the diameter of the focal spot is more than 1 μm, then the tube is called microfocus tube. Tubes with smaller focal spots are called nanofocus tubes. Smaller focal spot increases the image quality and the accuracy of the reconstruction (see *Imaging parameters and related physics* for more information). (Daneke & Schanklies, 2004)

Synchrotron sources produce X-ray beams with higher quality and intensity, but are much more complicated and larger devices than the ordinary X-ray tube sources. Synchrotron radiation is produced by accelerating electrons in vacuum and then undulating the electron beam by magnets. Initially, electrons can be produced like in the tube sources, by heating a filament from which the electrons are emitted forward. Emitted electrons are first accelerated nearly in the speed of light in a so called booster loop (figure 2) where the electrons are guided with magnets and accelerated by electrical fields. (Bilderback et al., 2005; Görlich, 2009) Once boosted, electrons are kept in a magnetic storage ring, and X-rays are produced in undulators when needed (Görlich, 2009).

Cathode

Grid

Centering stage

Electron beam

Focusing stage

Objective aperture

Target

X-ray beam
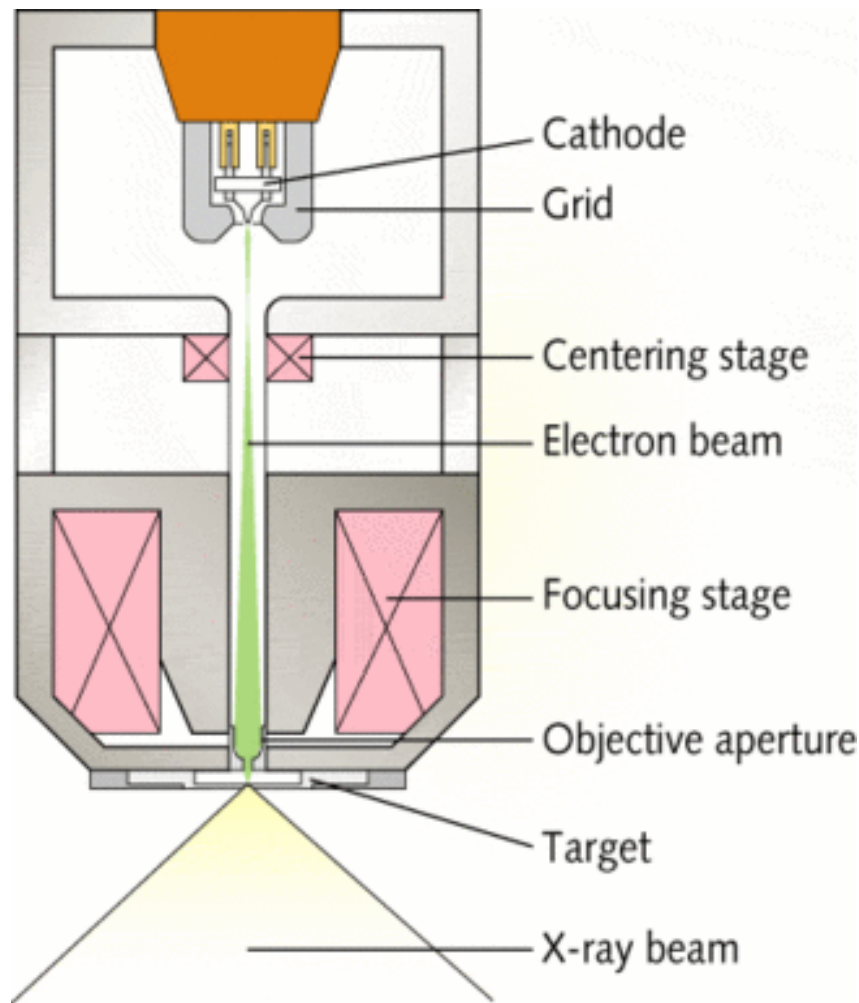
**Figure 1.** Cross-sectional representation of a microfocus X-ray tube. The cathode filament is heated up and electron cloud is produced behind the negatively charged grid. The tube is electrically lengthwise polarized and the electrons are pulled towards the positively charged transmission target made of heavy metal. Electrons are dosed through the grid and the beam is guided through different magnetic guiding stages. Small focal spot is formed inside the transmission target, electrons are slowed down by the interactions with the target atoms, which leads to emission of X-ray photons. Figure adapted from Daneke & Schanklies, 2004.

Undulators are arrays made from strong magnets and they produce periodically alternating magnetic pathways. In the moving frame of the emitted electrons the magnetic pathway looks like an alternating magnetic field with a certain $f$, which forces the electrons to oscillate up and down. As a result of the repeating acceleration and deceleration cycles, X-ray photons are emitted by the varying $E_{kinetic}$ the electrons experience. (Bilderback et al., 2005) Because of the accurate adjusting possibilities and other technical details, the synchrotron radiation can be highly monochromatic and coherent. The source spot is extremely small and greater intensities can also be reached than with the much simpler tube sources. (Yue et al., 2010; Bilderback et al., 2005) It is notable that the synchrotron sources are usually enormous, building sized systems (Görlich, 2009), although, research has been made for developing novel table-top synchrotron sources (Kneip et al., 2010).
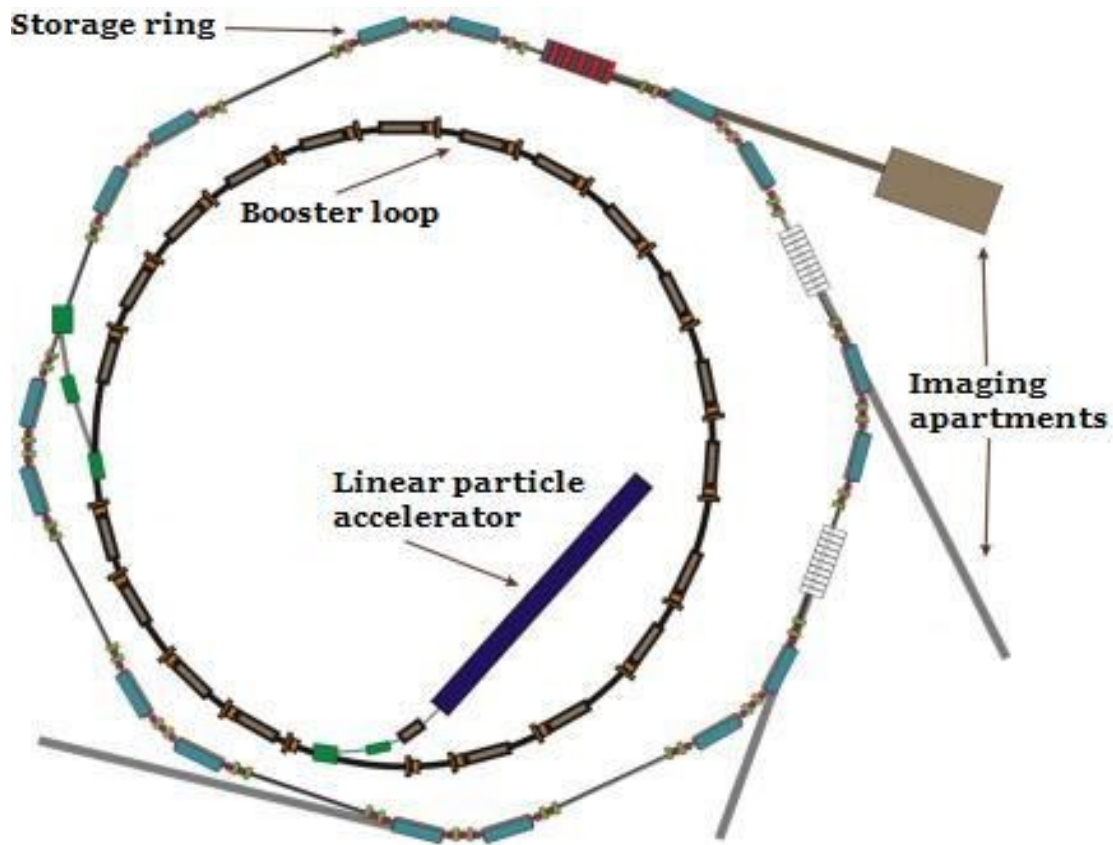
**Figure 2.** Illustration of a synchrotron radiation source facility. Electrons are first emitted from the linear particle accelerator and boosted in the booster loop. Then the accelerated electrons are guided into the storage ring, where they are finally guided into the undulators lying in front of the imaging apartments. Undulators undulate the electron beams, and X-rays photons are produced by the related acceleration and deceleration cycles. During the acceleration and storing, electrons are accelerated and guided with electrical field stages and magnetic benders respectively. Notice that the circumference of the storage ring can be over hundred meters. Figure adapted from Görlich, 2009.

## 2.1.2. Image capturing devices

Usually, μCT devices use charge-coupled devices (CCD) for digitalizing the acquired images (Holdsworth & Thornton, 2002; Cheng et al., 2011). The size of the CCD is nowadays in megapixel scale and the digitalization capability can be between 12 and 16 bits for example, providing shades of gray from 4096 to 65536 respectively (Brunkea et al., 2008; Kazakia et al., 2003; Voronov et al., 2013). CCDs themselves are not much sensitive to X-rays, why the X-rays are often converted into photons of visible light. This is done by a scintillator, a sheet of fluorescent material in front of the other light capturing devices (figure 3). The atoms in the scintillator become excited
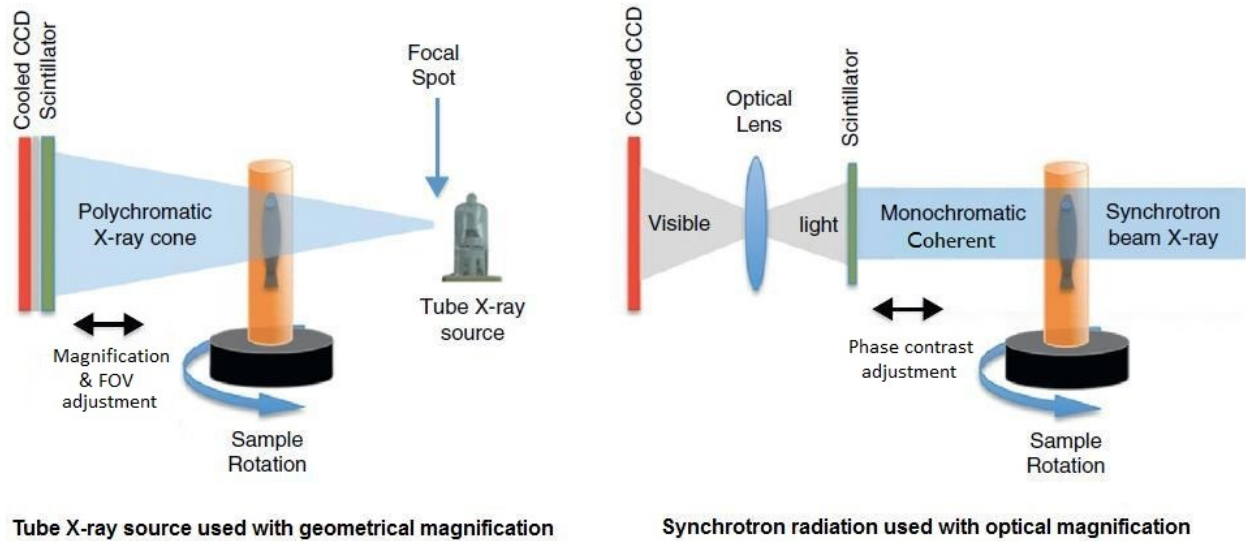
**Figure 3.** Schematic presentations from two different μCT imaging setups. An X-ray cone beam, produced by the tube source, is allowed to expand geometrically (left). After going through the sample, the X-ray photons are converted to visible light by the scintillator sheet and the image is digitalized by the CCD. By varying the source/detector distance ratio, the image can be magnified and the size of the field of view (FOV) changed. In the right side, the monochromatic and coherent X-ray beam from synchrotron source is guided through the sample and collided with the scintillator. The visible photon stream is modified by optical lenses and guided to CCD. Photon streams produced by the X-ray tube sources may also be magnified optically, after the energy conversion by the scintillator. Instead, coherent synchrotron X-ray beam does not expand much and the synchrotron based setups lack the possibility to use geometrical magnification. Because of the high beam quality of the synchrotron radiation, the stronger phase contrast effect can be adjusted by changing the detector distance. In all cases, CCD are cooled to decrease the internal thermal noise. Figure adapted from Cheng et al., 2011.

by the X-rays, and they emit visible photons which are guided towards the CCD. (Holdsworth & Thornton, 2002; Cheng et al., 2011; Eijk, 2003)

Visible photons, emitted by the scintillator, are guided directly to the CCD camera, or in some devices first through optical apparatuses. The magnification can be acquired by both the geometrical spreading of the applied X-ray beam and the optical magnification. With the highly coherent synchrotron radiation, the optical magnification is the only reasonable way to magnify the image, because the laser-like X-ray beams do not spread much. Cone beam X-ray images, produced by the tube sources, may also be further magnified by optical devices, but are not capable of producing images with strong phase contrast. Instead, coherent and monochromatic synchrotron radiation can be used for producing good phase contrast. Both the geometrical magnification and phase contrast can be adjusted by changing the source/detector distance ratios. (Cheng et al., 2011)

## 2.1.3. Imaging parameters and related physics

Basically, taking a single X-ray transillumination image is much like taking an ordinary photograph with a digital camera. There are many common things to consider for acquiring a good image, like how to compensate the loss of luminosity when higher zooms are used etc. There are still three main differences between photographing and taking a single image with µCT. First of all, in µCT imaging, the X-rays are transmitted through the imaged target before converting them to visible light. The contrast is formed by loss of the X-ray photons before they reach the scintillator; this is called attenuation contrast. The other contrast mechanism is the in-line phase contrasting, in which the distribution of wavelike behaving photons is varied by phase delays the refracted photons experience. Secondly, typical µCT devices lack the possibility to resolve photons with different wavelengths and the "colors of X-rays" cannot be distinguished. The µCT detectors either count a photon or not, and they can only produce grayscale images. As the third difference, the luminosity circumstances during µCT imaging can be comprehensively controlled in the performance range of the used source, if compared to using a flash or waiting a sunny day for taking a normal photo.

For making a good 3D reconstruction from the imaged target, the individual 2D images should be acquired carefully. The most important imaging parameters and their effects on the image quality are listed in the table 1 and the content of the table is considered more accurately in the following sub-sections. The used imaging settings are always tradeoffs between the different advantages. The different imaging results, and even imaging parameters, are interconnected; when varying one the other must also change. There can also be different views how to consider these relations, like how in the table 1 the larger detector distance is considered to decrease the attenuation contrast, as the larger penumbra blurs the interfaces arising from the attenuation differences in a sample. It could be rightly thought as well that the penumbra is not related to the attenuation contrast, as these two are different things. Thus, for simplicity, the table 1 and the following sub-sections are considered as general guidelines, rather than being presented as absolute truths.

**Table 1.** Effects of imaging parameters on imaging outcomes – relations between absolute numerical values

| Imaging parameters | | Photon count/SNR (2.1.3.1.) | Contrast | | Pixel size (2.1.3.4.) | FOV (2.1.3.4.) | 3D precision of reconstruction (2.1.3.5.) | Imaging time (2.1.3.6.) | Data size (2.1.3.6.) |
|---|---|---|---|---|---|---|---|---|---|
| | | | By attenuation (2.1.3.2.) | By phase shifting (2.1.3.3.) | | | | | |
| P=VI | $V_{acceleration}$ | ↑ | ↑↓ | ↓ | | | ↑↓ | ↓ | |
| | $I_{source}$ | ↑ | ↓ | ↓ | | | ↓ | ↓ | |
| | $P_{source}$ | ↑ | ↓ | ↓ | | | ↓ | ↓ | |
| Optical magnification | | ↓ | | ↑ | ↓ | ↓ | | | |
| Source distance | | ↓ | ↑ | ↑ | ↑ | ↑ | ↑ | ↑ | |
| Detector distance | | ↓ | ↓ | ↑↓ | ↓ | ↓ | ↑↓ | ↑ | |
| Exposure time | | ↑ | | | | | | ↑ | |
| Camera binning | | ↑ | | ↓ | ↑ | | | ↓ | ↓ |
| Spectral bandwidth (native X-ray without beam hardening) | | ↑ | ↑↓ | ↓ | | | ↑↓ | ↓ | |
| Number of images | | | | | | | ↑ | ↑ | ↑ |
| Degree of rotation | | | | | | | ↑ | | |

| | |
|---|---|
| Directly proportional relation | ↑ |
| Inversely proportional realtion | ↓ |
| Important relation which depends on other circumtances | ↑↓ |

## 2.1.3.1. Photon count and SNR

It is easy to understand that without any photons, it is impossible to acquire an image. Furthermore, because CCDs are non-ideal apparatuses, they produce small background noise in the images, which may disrupt the image quality in low luminosity conditions (figure 4A). The relation between the actual signal and the background noise is called signal to noise ratio (SNR). Without going into the details, SNR can be calculated generally by:

SNR = Signal amplitude/Noise amplitude          [5]

SNR should be as high as possible for distinguishing the actual signal from the noise. From the aspect of the µCT operator, the easiest way to increase the SNR is to keep the amount of photons so high that the intensity, seen by the CCD, can vary from highest brightness values to near zero. However, the saturation of the CCD, in other words over exposure, should be avoided, so that the intensity variations do not go over the usable resolving range. (Beutel et al., 2000)

Even with an ideal CCD, capable of counting every photon efficiently and accurately, one cannot produce clear images with low amounts of photons. This is due to quantum mechanical shot noise

effect, arising from the unsharp probability distribution of photons (figure 4B). If the amount of the acquired photons is too low, a couple of photons here and there will produce a grainy image. Furthermore, the sharp features of a sample cannot be digitalized accurately as the photons, representing the same feature, can land onto different pixels in the CCD. That is because the photons travel through the space-time as quantum mechanical probability waves rather than classically behaving, highly localized particles. (Feynman et al., 1966) Too dim X-ray beam can also lead to a situation where the photon stream is locally strong, but no photons go through the denser and thicker parts of the sample. Thus, samples containing both dense (or thick) and light (or thin) areas are problematic to image. The appropriate range of photon counts is hardware dependent and is usually provided by the μCT manufacturers. The final optimization is left for the μCT operator, who tests and sets the imaging parameters by taking single projection images before acquiring the actual data set.

The simplest way to increase the photon count is by increasing the source current ($I_{source}$). The current is related to the voltage and power by the simple formula:

$$P = VI \qquad\qquad [6]$$

Usually, X-ray sources have a maximum power limit, which cannot be exceeded without damaging the source. Thus, if a certain $V_{acceleration}$ limit is exceeded, the $I_{source}$ must be decreased and vice versa. The maximum and average energies of the X-ray spectrum are directly proportional to $V_{acceleration}$, because more Joules are invested in the $E_{kinetic}$ during the acceleration. Thus, by increasing the $V_{acceleration}$, it is more likely that an X-ray photon penetrates through the sample and increases the photon count seen by the CCD. Though, if the photons are too energetic, the intensity variation might vanish because too many photons go through the sample without any interactions (see *Contrast made by X-ray attenuation*). By increasing the $I_{source}$ the amount of the initially emitted X ray photons is increased, but their characteristic stays unchanged. Naturally, this increases the availability of photons for the digitalization. (Beutel et al., 2000)
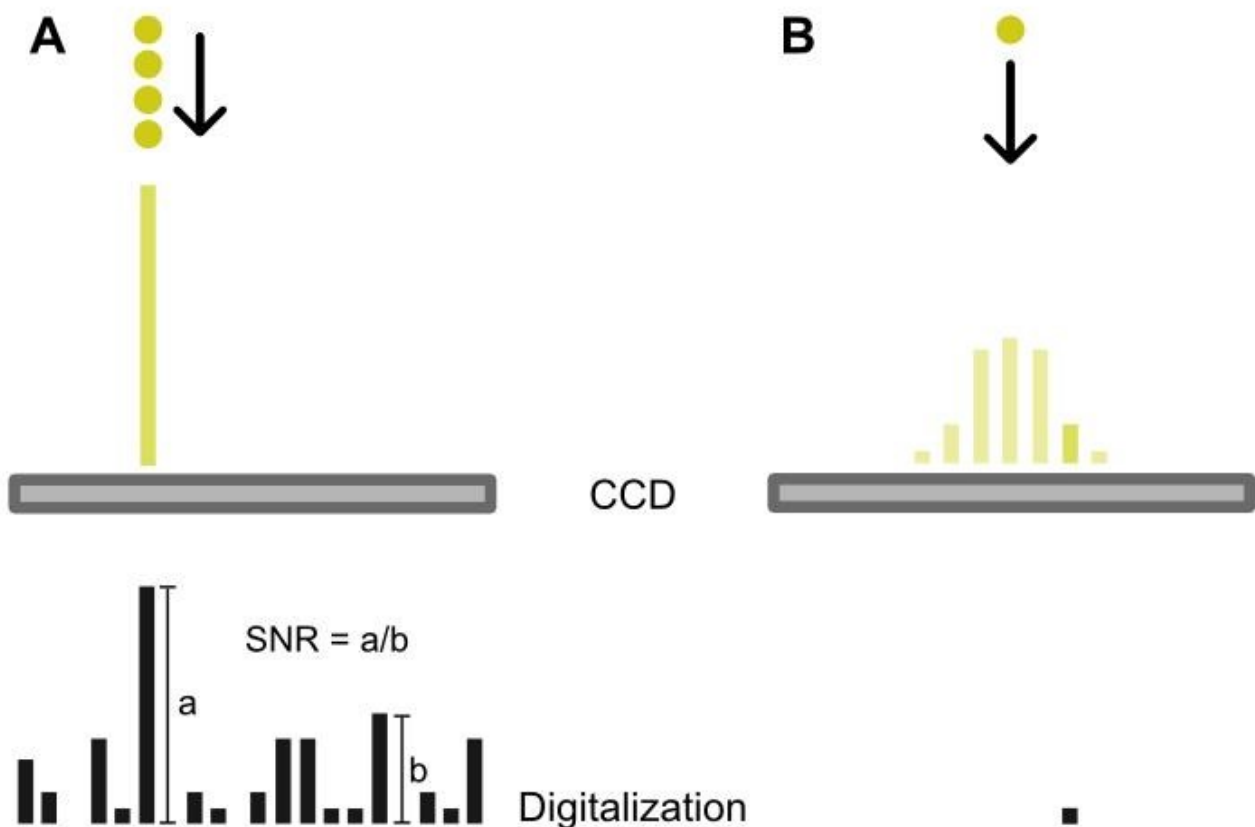
**Figure 4.** (A) Presentation from an unideal CCD (real) acquiring multiple, classically behaving (non-real), coherent photons, emitted from the same point source. The yellow vertical bars present the probability distributions of the photons and the black bars present the result of the digitalization. In this example, higher signal intensity means more photons. All of the photons are registered in one pixel, but the digitalization is corrupted by the thermal noise. The relation between the actual signal (a) and the maximum noise spike (b), SNR, is desirable to keep as high as possible for distinguishing the signal from the noise. The second figure (B) presents an ideal CCD (non-real), acquiring one photon which acts like a quantum mechanical probability wave, or a wave-particle (real), emitted from a point source. Light is fundamentally quantized, which is why the digitalization of small amounts of photons will produce grainy images (shot noise). The probability of finding the photon from a specific location in space spreads during the travel between the source and the detector. The spreading is further increased by the non-ideal optics, which can introduce dirt in the optical pathway. Dirtiness produces diffraction and can yield even separate landing areas where the singular photons can go. Thus, it is not statistically accurate to digitalize the image only by a couple of photons. On the other hand, the wave-particle nature of photons can be exploited for phase contrast imaging (see *In-line phase contrast imaging*).

The use of higher optical magnification decreases the amount of photons arriving at the CCD, since the lenses force the photons to spread on larger areas. Increasing the source and detector distances also decreases the photon counts, since there is more space for the beam to spread. This also includes coherent synchrotron radiation, since every source is more or less non-ideal, but the effect is much smaller than with the X-ray tube sources. Longer exposure time naturally increases the photon count, since there is more time for acquiring photons. Camera binning is the ability to count photons with multiple adjacent CCD sensory cells into same virtual pixel. Thus, the use of higher camera binning increases the photon count for a single virtual pixel. (Beutel et al., 2000)

X-ray beams can be filtered easily by using certain media, for example aluminum, for absorbing photons with lower $E_{photon}$. This is called beam hardening. Filtering decreases the width of the energy spectrum and also the total amount of photons available for transillumination. (Beutel et al., 2000)

### 2.1.3.2. Contrast made by X-ray attenuation

The word "contrast" simply means how clearly different features are distinguishable from each other. In other words, how steep are the intensity or color differences between the features. Like noted earlier, the color contrast is not available in μCT imaging, since regular μCT devices cannot resolve different wavelengths from each other. When discussing about the attenuation contrast in native soft tissues, the photoelectric effect has the major influence on the photons having energies less than 20 keV. With the higher energies the role of Compton scattering becomes bigger. (Kalender, 1992) Compton scattering might increase noise as the angle of scattered photons can be large and if the photons do not miss the detector. Instead, the photoelectric effect totally vanishes photons without smearing the forming image. The likelihood for a photon to become absorbed increases if the $E_{photon}$ matches the binding energy ($E_{binding}$) of an electron in an atom or molecule. Thus, non-dense samples are better to image with low acceleration voltages, while contrasted or otherwise dense materials can irreversibly absorb even the high energy photons, still preserving the image quality. (Seibert & Boone, 2005)

The easiest way to gain the attenuation contrast is to adjust the imaging parameters so that sufficient amount of X-ray photons will become absorbed in the sample. As a general rule, $V_{acceleration}$ is inversely related to the efficiency of attenuation contrast. That is because decreased $E_{photon}$ is closer to the $E_{binding}$ of the lower electron shells in usual elements found in biological structures, like carbon, nitrogen and oxygen. Thus, with the spectrum of low average energy, it is more likely that the spatial absorption rate will vary even because of minor elemental variations in a sample, whereas too energetic X-ray photons may pass the sample without any interaction. Though, the higher net absorption likely increases the time needed for acquiring acceptable amounts of photons.

On the other hand, the absorption will increase also in gradual manner if the $V_{acceleration}$ is increased. This phenomenon occurs when the $E_{photon}$ exceeds the $E_{binding}$ of higher electron shells (figure 5). The K-shell electrons have the highest $E_{binding}$ in an atom, and in heavy elements might match with the high X-ray photon energies. For example, like simulated in the figure 5, good X-ray absorption in elemental iodine ($I_2$) is gained if the $V_{acceleration}$ is around 58 kV. That is because most of the photons in the X-ray spectrum has the energy close to the 33.2 keV which correspond the $E_{binding}$ of the K-shell electrons (or $E_{K-edge}$) in iodine. If the $V_{acceleration}$ is increased more, the right-hand tail of the X-ray spectrum moves towards higher values and becomes thinner and longer. This leads to higher amounts of photons with too large $E_{photon}$, which are not absorbed efficiently anymore. (Seibert & Boone, 2005)
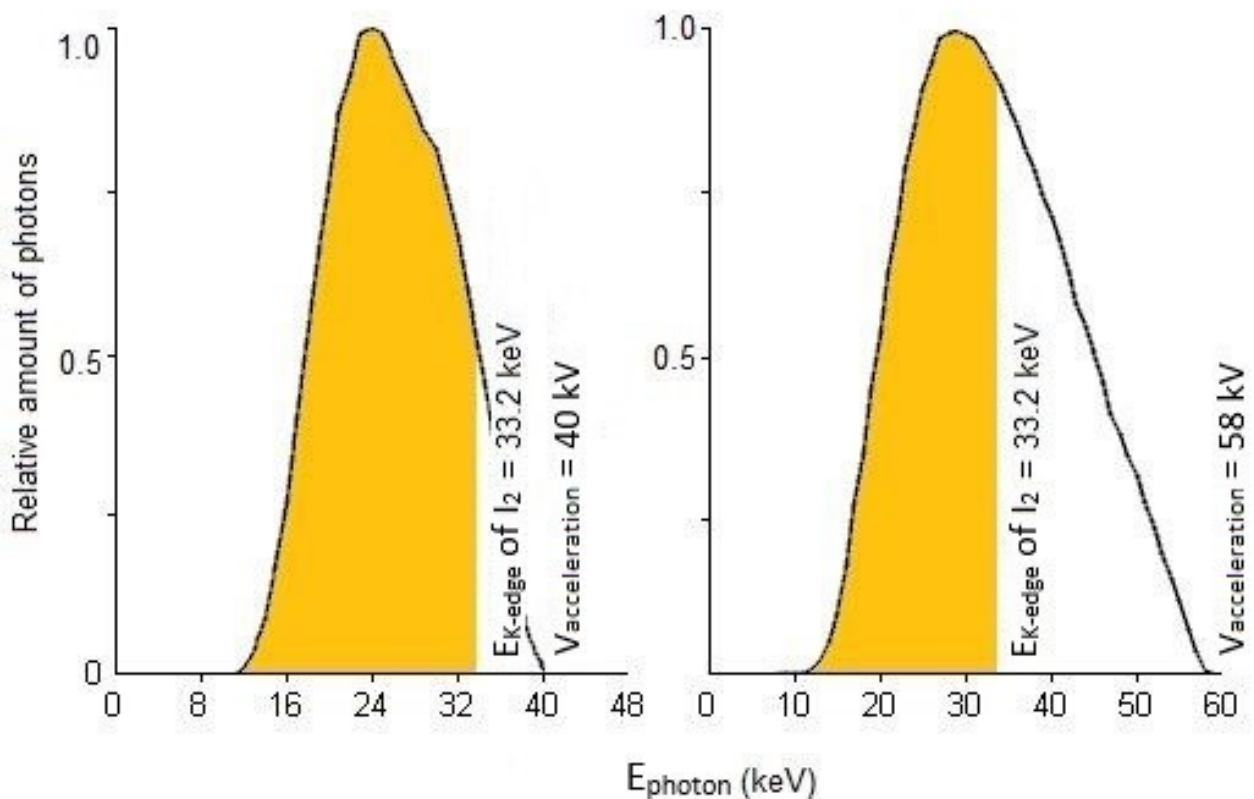


**Figure 5.** Simulated X-ray spectrums when different $V_{acceleration}$ are used in a virtual tube source with a tungsten filament. In the left-hand graph the $V_{acceleration}$ is 40 kV. In the right-hand graph the $V_{acceleration}$ is 58 kV. The X-ray spectrum produced in an X-ray tube is polychromatic in nature and most of the photons have smaller $E_{photon}$ than the $V_{acceleration}$ can provide. Even without mathematical integration, it can be seen that the spectrum of the right-hand graph has more photons over the $E_{K-edge}$ of $I_2$ (33.2 keV). Thus, it is more likely that this type of radiation enhances the visibility of $I_2$ more than the radiation with the left-hand spectrum, because more photons have enough energy for knocking electrons out from the $I_2$-K-shells. Graphs adapted from Boone et al., 1998.

In practice, because the focal spot is never infinitely small, a so called penumbra is always produced on the surface of the sensor (figure 6). If the penumbra is small enough, it does not necessarily cover multiple rows of pixels why the interfaces of the imaged features are preserved. Enough large penumbra smears the boundaries and, thus, can be thought to decrease the contrast. In the worst case, large penumbra may blur the whole image and result only a flat, grey image. The size of the penumbra can be decreased by increasing the source/detector distance ratio. The size of the focal spot can also be slightly decreased by decreasing the source power ($P_{source}$). (Beutel et al., 2000) Practically, this means that the $I_{source}$ is decreased, because the $V_{acceleration}$ is usually already adjusted according the demands for acquiring good contrast.
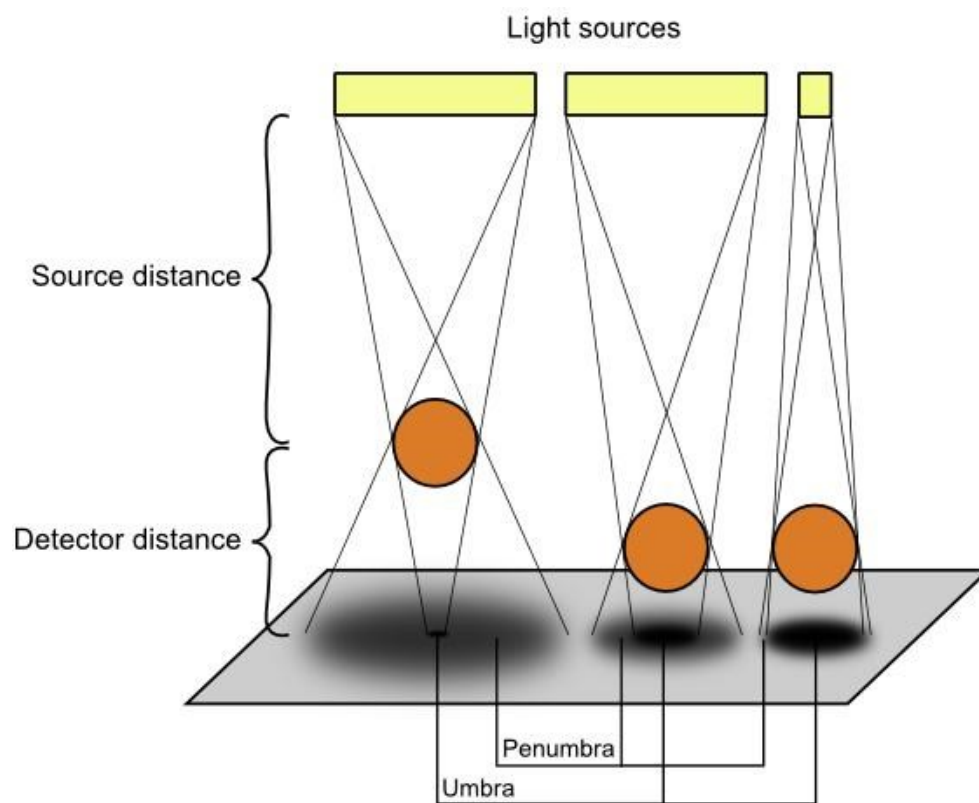


**Figure 6.** Illustration about the penumbra and the resulting unsharpness. Three light sources (yellow) radiate light against a flat detector (grey). Identical objects (orange) are placed between the detector and the sources. For simplicity, the pathways of light do not overlap between the each source. By following the thin lines between the sources and the detector, one can follow where the light reaches from the extreme ends of the sources. In the left-hand case the source/detector distance ratio is relatively small and the source is big. This results in large penumbra and, thus, a blurry image. In the center case, the object is closer to the detector and the size of the penumbra decreases. In the right-hand case, the size of the source is smaller, which leads to even smaller penumbra and a sharp image. It can also be seen that the geometrical magnification decreases, the circumference of the shadow becomes smaller, as the source/detector distance ratio increases.

### 2.1.3.3. In-line phase contrast imaging

In-line phase contrast method enhances the visibility of boundary areas in an image. Phase contrast is an ideal method for detecting structures when the samples are light and homogeneous in density. Still, at least moderate differences between the refractive indices must be present in the sample for successfully forming the image. Phase contrast is based on the phase shifts of spatially coherent, wavelike behaving photons and their interferences after the boundaries of materials result aberrations (figure 7). (Feynman et al., 1966; Gao et al., 1998).

The idea in the phase contrast can be boiled down into case where only two pathways for photons are considered at a time. Two closely and parallel traveling photons, which are perfectly in phase, will constructively interfere with each other, if their pathways are optically equally dense (figure 7). It is likely for the photons, or the singular photon in multiple pathways at the same time, to get absorbed there where the constructive interference occurs in the detector. That is because the photons move through the space-time as probability waves rather than classical, highly localized particles; the increasing amplitude in the quantum wave increases the probability to find the corresponding photon. Instead, if the pathways are different and the other one includes interfaces of different refractive indices, the non-uniform medium bends the trajectory. This means that some of the photons in the beam travel shorter pathways, while the others travel longer. This inequality leads to phase shifts between originally coherent photons and formation of an image as the wave amplitude and photon counts drop in places. (Feynman et al., 1966)

Because the focal spot is not infinitely small, it produces penumbra which disrupts the possible interference patterns seen by the detector. Like noted in the previous section, the size of the penumbra can be decreased by increasing the source distance (figure 6), why the source distance is directly proportional to the strength of the phase contrasting. (Beutel et al., 2000) Furthermore, larger source distance increases the spatial coherency by the simple geometry; the spreading radiation front starts to resemble a plane wave as the distance from the source increases, which enhances the phase contrasting. The size of the focal spot can be decreased by decreasing the $P_{source}$ and its directly proportional partner $I_{source}$, which reduces the blurriness made by the penumbra effect.
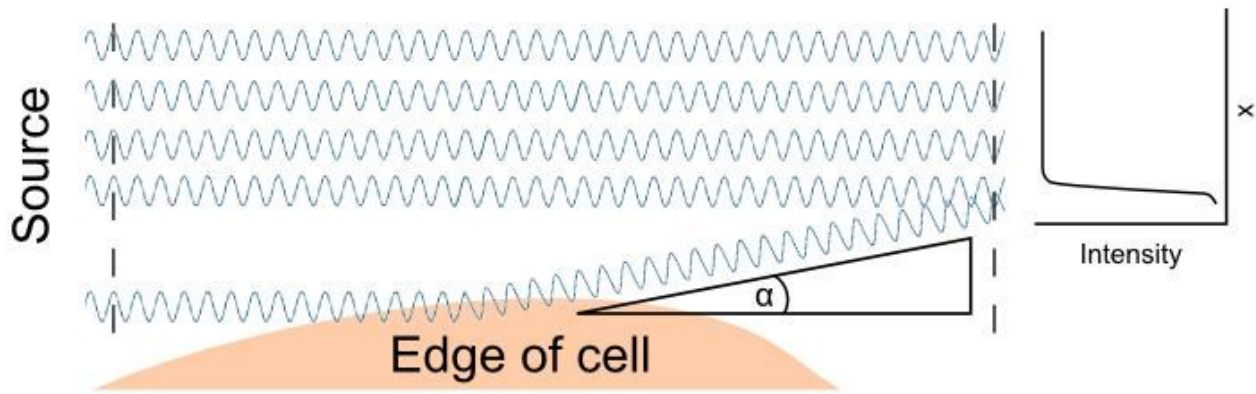
**Figure 7.** Highly simplified presentation how the phase contrast occurs. The photon source (left) emits coherent beam of radiation; the photons in the five pathways are perfectly in phase in the beginning. The black dashed lines are drawn for making it easier to see the state of coherence. Most of the photons travel through the homogenous medium (above), in which the cell (below) is embedded. None of the photons in the pathways become absorbed between the dashed lines, why the attenuation contrast does not give any information about the sample. Photons in the lowest pathway interact with the surface of the cell and aberration occurs. The angle of the new trajectories depends on the surface structures of the cell. Only one new route is presented with the angle α. In the chosen depth after the sample (the rightmost dashed line), destructive interference occurs between the two lowest pathways. In this point of space the detector would see a drop in the light intensity as the likelihood of photons being absorbed in the corresponding pixel decreases. If only a single photon will be emitted at the beginning, and it travels through the all pathways like wave-particles can do, it would become absorbed with the equal probability in some of the pixels after the three uppermost pathways, while there is zero probability for the photon to hit in the pixel behind the lowest two pathways. Because the absorption probability decreases in the ends of the nearest pathways of the cell surface, the interface between the cell and the medium is now enhanced, while no photons were absorbed.

Because the detector distance may be too small for having effective phase shifting, and on the other hand too large which separates the origin of aberration and the final point of absorption in CCD, the relation between the detector distance and the phase contrasting are bidirectional. (Gao et al., 1998)

The chromatism is also an important factor in the phase contrast imaging. Photons with different λ will refract differently and smear the diffraction patterns of each other. That is why it is not so easy to make phase contrast imaging with polychromatic tube radiation. By beam hardening the radiation with filters the X-ray spectrum can be narrowed. (Gao et al., 1998, Boone et al., 1998) Lower $V_{acceleration}$ will also produce narrower X-ray spectrums, why the $V_{acceleration}$ is inversely proportional to the strength of the phase contrasting (figure 5; Boone et al., 1998). Furthermore, the wave features of photons become enhanced by lowering $E_{photon}$ (formula 3) which further increases the phase contrast efficiency. (Feynman et al., 1966)

Optical magnification spreads the interference fringes away from each other. Thus, narrow intensity variations can be seen easier by using higher magnifications. If multiple CCD cells are combined to

a bigger, virtual pixel, the interference patterns could be lost inside of it. Therefore, binning and the strength of the phase contrasting are inversely proportional to each other.

## 2.1.3.4. Pixel size and FOV

Intuitively, higher optical zoom decreases the pixel size. Higher geometrical magnification, i.e. lower source/detector distance ratio, also decreases the pixel size (figure 6). Finally, higher camera binning increases the pixel size, which is quite obvious when multiple pixels are combined together to form a bigger virtual pixel. FOV is directly proportional to the pixel size when the imaging parameters, other than binning, are adjusted, because FOV is actually as large as the size of the detector matrix multiplied by the pixel size. Thus, it is impossible to gain the best possible accuracy at the same time with the widest possible FOV. For having large FOV with high resolution, depending on the used hardware, one can compose the final data set by taking multiple sub-imaging.

## 2.1.3.5. 3D precision of reconstruction

In this context, the 3D precision of reconstruction means how good is the position correlation between the real, physical feature in a sample, and its virtual digitalized version in the virtual voxel matrix. Hence, this accuracy also refers to resolution, sharpness and other image quality factors, which all show how well the structural information is copied from the physical object into the memory of a computer.

Like stated earlier, the diameter of the focal spot increases with the increasing $P_{source}$, which further leads to decreased reconstruction accuracy (figure 6). Smaller source/detector distance ratio also contributes in the formation of penumbra, which is why the larger source distance and the smaller detector distances increase the reconstruction accuracy. Though, because the effect of the detector distance is bidirectional in phase contrasting, its effects on reconstruction precision can eventually be thought as bidirectional (Gao et al., 1998).

Unintentional beam hardening may also contribute into the reconstruction accuracy. Low energy photons may be filtered out before they reach the internal parts of the FOV, depending on how deep in the sample the FOV is. The possible sample container and the immersion solution, if there is such, may also absorb the photons with low $E_{photon}$ before it is intended. For example, if the outer areas of the FOV absorb all the low energy photons before the inmost area of the FOV is reached, it disrupts the reconstruction data by producing rim like artefacts, called beam hardening artefacts. (Beutel et al., 2000). $V_{acceleration}$ and filtering effects on the formation of contrast like described earlier, why they are eventually in bidirectional relation with the reconstruction accuracy. Finally, it is easy to understand that the amount of 3D structural information increases if the sample is imaged many times and from many different angles. Thus, more images, taken from many different angles, and the larger degree of rotation enhances the reconstruction accuracy.

## 2.1.3.6. Imaging time and data size

It is good to keep the duration of μCT imaging as short as possible for decreasing the risk of sample movement. Sample movement during the imaging contributes to the reconstructions inaccuracies and may bother especially with the non-rigid, soft material samples. The sample movement is especially troublesome if high resolution images are acquired. Also, because of the long imaging procedures, the availability of the μCT devices for multiple imaging projects decreases. There are two good ways to decrease the time needed for μCT imaging: collect less amount of images or decrease the time needed for acquiring singular images.

As stated earlier, sufficient amount of photons is needed for producing an image, which requires varying amount of time. If the $V_{acceleration}$ is increased, it is likely that higher amount of photons will pass through the sample. The amount of initially emitted photons can be increased by increasing the $I_{source}$, which contributes also to the amount of photons collected by the detector. If the spectral bandwidth is narrowed by filtering, the amount of photons that reach the sample in the beginning is decreased. Naturally, this contributes also to imaging time.

Especially in the X-ray tube source based µCT devices, the total distance between the source and the detector is directly proportional to the imaging time. If the total distance is increased, the spread of the cone beam, hitting against the detector, decreases the amount of the available photons for the digitalization (figure 3). Thus, both detector and source distances are directly proportional to the imaging time. Longer exposure time naturally increases the total imaging time. Higher binning decreases the imaging time, since the sensitivity of the CCD is increased by the virtual pixels owning larger surface areas. Taking more images elongates the whole procedure time, thus, the number of images and the imaging time are directly proportional to each other.

Without any hardware or time restrictions, it would be good to gather imaging data as much as possible. Only the limited storing space and the processing capabilities set the maximum size for the acquired data. The amount of data can be decreased only by taking fewer projections and using higher binning.

# 2.2. Non-specific and specific contrasting

## 2.2.1. Contrast agents

Soft tissues and other non-dense materials with low density variations are somewhat problematic to image with µCT, because high energy X-ray photons go likely through the materials without any interactions. Instead, mineralized tissues are easy to image without contrasting agents at all, even small and fine details are distinguishable in native samples (Appel et al., 2013; Yue et al., 2010; Kazakia et al., 2003; Metscher, 2009). Like noted earlier, X-ray attenuation increases by the increasing sample density, which is the origin of the basic contrast in X-ray techniques. Basically, any enough dense substance can be used as contrast agent for increasing the effective density of the sample. It is necessary that the substance attenuates X-rays more than the sample itself, otherwise the effective attenuation in a sample does not change. Hence, good elements to be used as contrast agents have atomic numbers usually well beyond those of hydrogen, carbon, nitrogen and oxygen which are the most abundant elements in living organisms. These are common elements in human body for example (Seibert & Boone, 2005), and carbon and oxygen are also common elements used

in biopolymers (Thimm et al., 2012; Zehbe et al., 2010; Dorsey et al., 2009; Voronov et al., 2013; Nelson et al., 2011; Watlinga et al., 2010).

Contrasting agents can be divided into three main categories: non-specific background stains, semi-specific and specific stains, later also called labels. Background contrasting enhances the general features of a sample. In the simplest case, a background staining can be performed by simply immersing the sample in the staining solution and by letting the contrasting agent to diffuse inside. The distribution of the contrast agent, and hence how the contrast enhances, depends on the varying chemical properties in a sample. Specific labelings, however, can reveal even the finest molecular details and their distributions. This is done by exploiting the highly specific, intermolecular complementarities between antigens and antibodies, for example. Thus, by background stainings one can distinguish several soft tissues from each other at once, and with the specific staining study distributions of particular molecular details. In this thesis, a so called semi-specific contrasting methods are also categorized and discussed. Semi-specific stains fall between the earlier two categories, as the semi-specific contrasting can be used for distinguishing somewhat specific structures, but they lack the extreme accuracy of the specific stains. In some cases a certain contrasting agent may work like a background stain, and with other types of samples like a semi-specific stain.

Many different elements are used as contrast agents. Iodine (Stephenson et al., 2012; Jeffery et al., 2011; Cox and Jeffery, 2011; Pauwels et al., 2013; Metscher, 2009), PTA (Metscher, 2009; Pauwels et al., 2013), tungsten (Metscher, 2009; Pauwels et al., 2013) and osmium (Metscher, 2009; Hann et al., 2011; Watlinga et al., 2010; Ruan et al., 2013; Dorsey et al., 2009) are probably the most used elements for making non-specific contrast agents. Molybdenum, iron, zinc, mercury and lead are also used for making background contrasting (Pauwels et al., 2013), but they are used less than the previously mentioned ones. Silver (Ag), gold (Au) and iron oxide (FeO) particles are more common substances for making specific and semi-specific contrasting (Metscher & Muller, 2011; Chien et al., 2013; Thimm et al., 2012; Zehbe et al., 2010; Eck et al., 2010; Hainfeld et al., 2011).

## 2.2.2. Non-specific background contrasting

Without the varying chemical interactions within a sample, the contrasting agents would be useless. Perfectly even distribution would give flat X-ray images and no structural information could be acquired. The mechanisms of interactions depend on the chemical nature of the used contrast agents. For example, the distribution of $I_2$ is mainly determined by hydrophobic interactions (Robyt, 1998) and covalent additions by halogenation reactions (Hamilton, 1997; figure 8). Good hydrophobic phases in biological samples for $I_2$ to interact are, for example, hydrophobic cores of amylose double helices in plant tissues (Robyt, 1998), while unsaturated lipids are common targets for halogenation reactions (Hamilton, 1997). Usually, elemental iodine is dissolved in absolute ethanol, why the solution is called I2E. The use of I2E stain is suitable continuum for histological samples which are conventionally transferred to absolute ethanol before embedding into paraffin blocks for further sectioning with a microtome (Bancroft & Gamble, 2008).

Instead, and like the name implies, the anionic forms of iodine, for example iodide ($I^-$), have electrostatic interactions within a sample, rather than hydrophobic or covalent ones (figure 8). Thus, $I^-$ likely localizes in places where positive counter charges and appropriate chelators are present, and it should repel negatively charged structures like glycosaminoglycans (GAG; Joshi et al., 2009). Usually, $I^-$ is applied in the form of potassium iodide (KI) salt. So called Lugol's solution, shorter IKI, includes both the $I_2$ and KI. In clinical environment, IKI solutions are used as disinfectants, but they are successfully applied also as background stains for µCT imaging. (Jeffery et al., 2011; Metscher, 2009) Because of its chemical versatility, IKI stain could reveal more structural features than the $I_2$ and KI alone. Naturally, if this is the case, then IKI staining should be preferred over these mono-agent stains. If the contrast is decreased because of too comprehensive distribution of iodine, then I2E or purely KI based stains could be better choices.

There are also other technical aspects to consider when comparing and choosing between different iodine based stains. For example, as amphiphilic solvent, ethanol based I2E stain might have faster penetration into sample than the water based IKI does. Ethanol itself works also as preservative and somewhat as fixative by precipitating and coagulating proteins (Bancroft & Gamble, 2008). In the simplest case, the iodine based staining can be performed just by immersing and saturating the samples by the chosen stain. Finally, samples are washed with the used carrying solution in which

the contrasting agents were dissolved or the samples are imaged in the staining solution itself. Practical imaging examples of the iodine based contrast enhancements are presented in the figure 9. (Metscher, 2009)

PTA forms highly acidic complexes made of oxygen, phosphorus and tungsten. Because of its acidity, some of the PTA complexes can have high negative charge, even as high as -10 at pH 3.5 (table 2). PTA complexes are assembled and dissembled dynamically, and the complexes can change their size and unit charge, depending on the surrounding pH. (Zhu et al., 2003) Thus, by adjusting the used pH one can adjust the size and charge of the PTA complexes and possibly affect how they distribute. The diffusion of PTA is slower than that of the $I_2$ and KI based stains, even if applied with 70% ethanol for disrupting cell membranes and other lipid based obstacles for diffusion. In small enough samples, like the ones presented in the figure 9, slow diffusion is not a problem. In bigger samples the staining times could become unreasonable long, which sets practical size restrictions for samples intended to be stained by PTA. Like with the IKI and I2E stains, it is also possible to perform PTA contrasting by simply immersing the sample in the PTA solution. (Metscher, 2009)
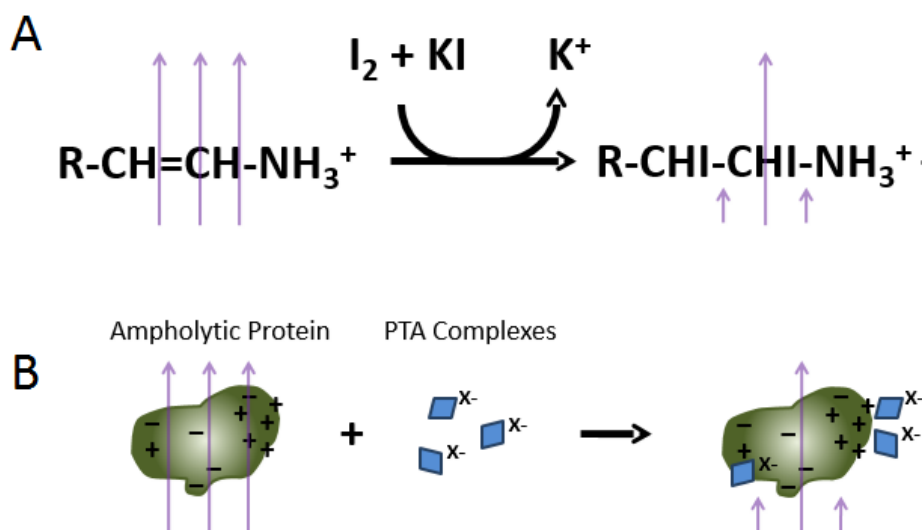


**Figure 8.** Illustration of the main mechanisms how the IKI (A) and PTA (B) distribute in samples. In the case of IKI, the strongest and irreversible contrasting interaction is the halogenation reaction between the unsaturated structures and the $I_2$ molecules (A). $I_2$ molecules may also be trapped inside the hydrophobic phases of a sample (not presented in the illustration), but these interactions are more reversible. Hence, the $I_2$ signal, without the halogenation attachment, might start to fade if the sample is not imaged in the staining solution itself. Likewise, $I^-$ anions of IKI might also fade away if the samples are imaged in non-contrasting solution. $I^-$ distributes by the electrostatic interactions, as $I^-$ changes its primary counter cations, $K^+$, to ones provided by the sample, positively charged amine group in this example. In B, the negatively charged PTA complexes interact with the ampholytic protein found in a sample. The protein has enough strong positive surface charges which attract the PTA complexes. As a reminder, μCT cannot directly resolve these kind of nano-scale distributions described here, but if the distribution heterogeneity have also macroscopic contribution, then the illustrated contrasting mechanisms will also enhance X-ray contrast for μCT imaging.

**Figure 9.** Virtual cross-sections from the µCT imaged hind limb buds of chick embryos. Samples were imaged either unstained and after different background contrasting were done. The unstained sample is almost as dense as the surrounding ethanol. All of the shown stains gave good contrast, but different contrasting agents were distributed somewhat differently. Overnight immersion in the contrasting solutions was enough for comprehensively staining the samples in which the inmost parts were approximately 500 µm away from the surfaces. The spatial resolution is approximately 12 µm and the 2D images were acquired by using polychromatic tube radiation with the 40 kV acceleration voltage. Figure adapted from Metscher, 2009.

**Table 2.** Principal components of PTA in aqueous solutions with varying pH.

| pH | Principal Components of PTA |
|----|----------------------------|
| 1.0 | $[PW_{12}O_{40}]^{3-}$ |
| 2.2 | $[PW_{12}O_{40}]^{3-}$, $[P_2W_{21}O_{71}]^{6-}$, $[PW_{11}O_{39}]^{7-}$ |
| 3.5 | $[PW_{12}O_{40}]^{3-}$, $[P_2W_{21}O_{71}]^{6-}$, $[PW_{11}O_{39}]^{7-}$, $[P_2W_{18}O_{62}]^{6-}$, $[P_2W_{19}O_{67}]^{10-}$ |
| 5.4 | $[P_2W_{21}O_{71}]^{6-}$, $[PW_{11}O_{39}]^{7-}$, $[P_2W_{18}O_{62}]^{6-}$ |
| 7.3 | $[PW_9O_{34}]^{9-}$ |
| 8.3 | $PO_4^{3-}$, $WO_4^{2-}$ |

## 2.2.3. Semi-specific contrasting

In some cases there is no clear way to categorize contrasting either to background or specific ones. With certain samples, contrast agent could behave like a background stain, giving comprehensive contrast all around the sample, and in other types of samples the same agent may target against a more confined group of structures. In the latter case, the distribution of the used contrast agent is not determined by the highly specific, intermolecular complementarities, but still the stain could be used for revealing somewhat specific, molecular structures of tissues (Joshi et al., 2009) or even for resolving phenotypic details between tumorous cells and otherwise healthy tissues (Hainfeld et al., 2011).

If halogenated to larger, positive molecules, iodine can be distributed also as positive ions. For example, these positive forms of iodine can be used as semi-specific stains for studying GAG distribution in articular cartilage. (Joshi et al., 2009) Colloidal metals as such could also be used as semi-specific stains. For example, it is shown that when intravenously applied in mice, bare 15 nm Au nanoparticles can localize into superficial areas of tumors in mice produced by human derived breast cancer cells (figure 10; Hainfeld et al., 2011).

For intravascular contrast agents, it is necessary to ensure that the stain remains in the vessels long enough before the µCT examination. Naturally, the required stability depends on the duration of the experiment and how long test animals are kept alive before reaching the imaging phase. Intravenous stability of colloidal metals can be adjusted by a couple of methods; by changing the size of the particles and by using different surface coatings. First of all, every blood circulating components are susceptible to become filtrated through the kidneys, if the component is physically small enough. Usually, particles with diameter >5 nm are not renally excreted, but metal nanoparticles are also susceptible for scavenging by macrophages, for example. Polyethylene glycol and polyvinylpyrrolidone coatings can increase biostability of these particles and, thus, keep them in the blood stream for longer periods of time. (Eck et al., 2010)

In the case of biomaterial-cell hybrid samples the use of semi-specific stains can give successful results for resolving individual cells with the ease and low cost of non-specific contrasting, but with
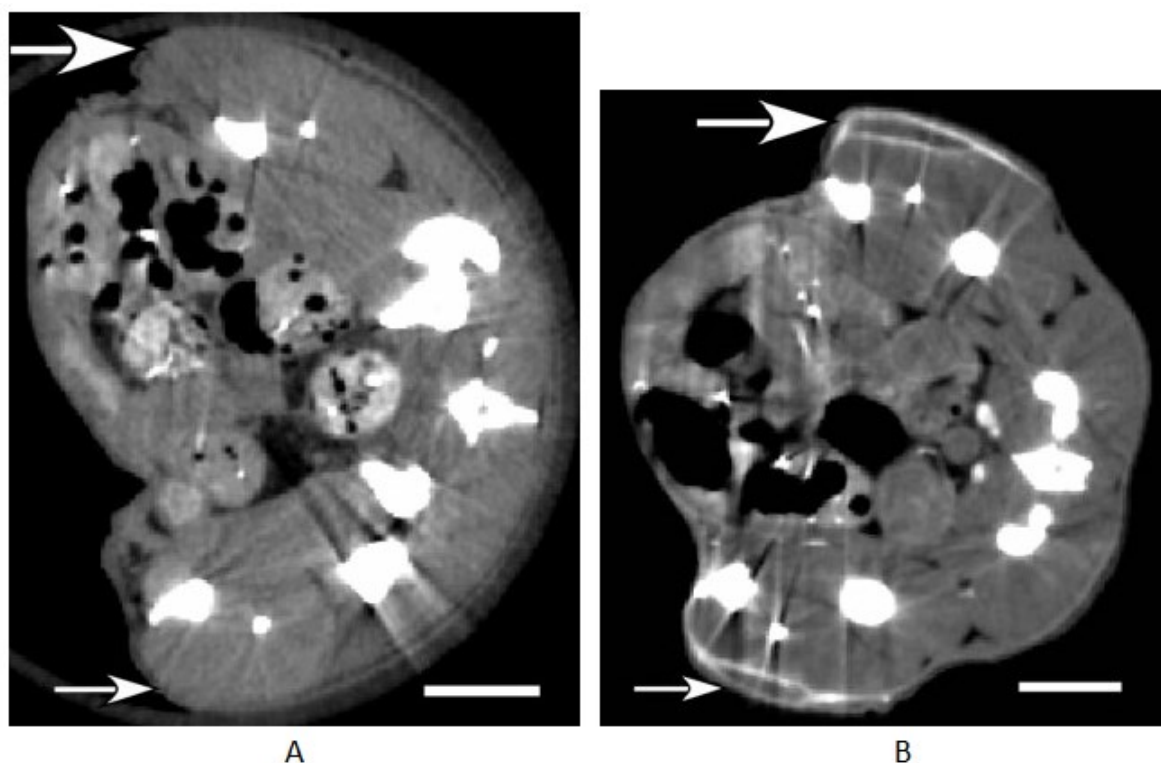
**Figure 10.** μCT section images from mice with the implanted human epidermal growth factor receptor 2 positive (Her2+; large arrows) and Her2- (small arrows) human cancerous cells. The figure A shows a section from the control mouse with no contrast agent treatment. The figure B shows the mouse which was injected with bare 15 nm Au nanoparticles (1.1 g Au kg $^{-1}$), scarified after 20 h and μCT imaged. As it can be seen the X-ray absorption of soft tissues is highest around both of the human derived tumors in B. Other high intensity signals arise from the dense bone tissues and the mineral containing food inside the intestines. The spatial resolution is 15 μm and the 2D images were acquired by using polychromatic tube radiation with the 45 kV acceleration voltage. Scale bars are 5 mm. Figure adapted from Hainfeld et al., 2011.

almost the same accuracy of antibody stains. For example, it is possible to use a so called Au-lysine staining for resolving embedded cells from gelatin gel matrices (figure 11; Zehbe et al., 2010). Lysine is proteinogenic amino acid, which has positive charge under physiological pH and pH lower than that. Thus, lysine gives positive surface charge for the conjugated metal nanoparticles and makes them attracted to any negative charges found in cells, like to DNA and anionic surface structures for example. Cells can be resolved from gelatin scaffolds by first making the conventional formaldehyde fixation in phosphate buffered saline (PBS). After the fixation, samples are washed from the excess aldehydes and are neutralized by glycine and bovine serum albumin (BSA). Before Au-lysine treatment, samples are transferred in double distilled water (ddH$_2$O) and the pH of the coming Au-lysine staining solution is decreased to 2 by hydrochloric acid for ensuring the positive surface charge of the applied particles. After the overnight staining at 4 °C, samples are washed with ddH$_2$O and a commercial silver-enhancement kit is used for reducing silver onto transported Au particles. (Zehbe et al., 2010)
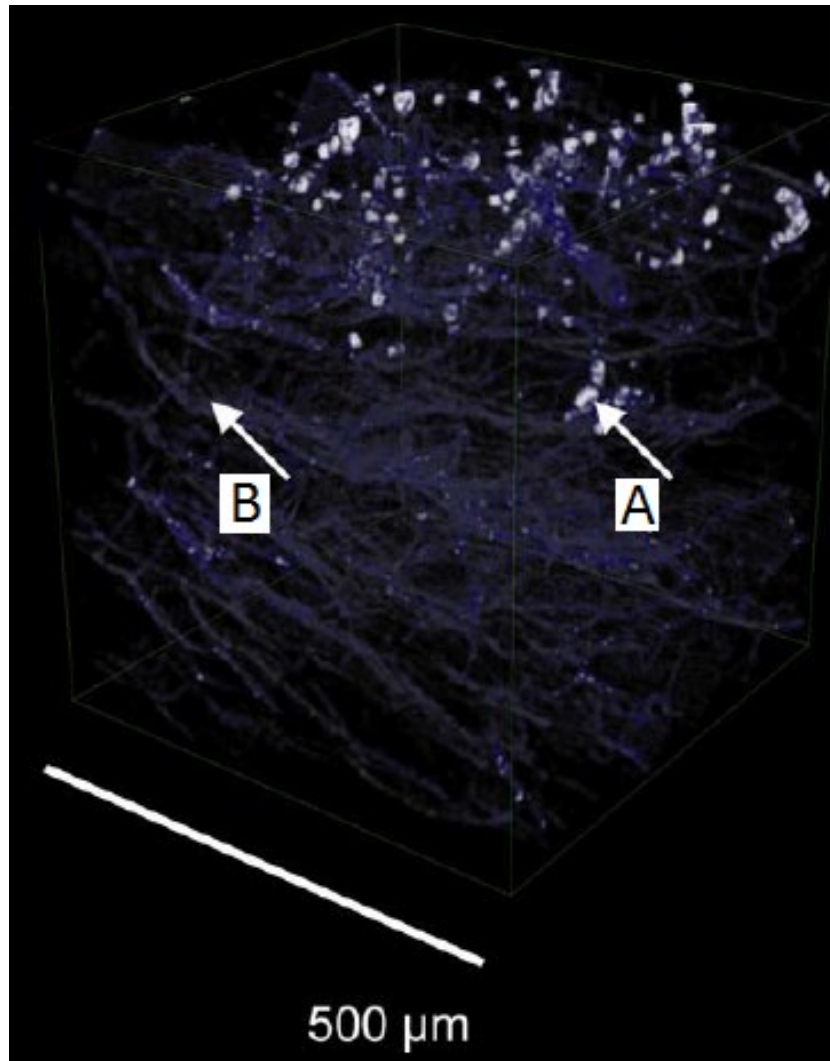
**Figure 11.** 3D μCT-reconstruction from Au-lysine stained cartilage cells (A) cultured in freeze-dried gelatin scaffold (B). The estimated spatial resolution is 3.7 μm and the 2D images were acquired by using monochromatic synchrotron radiation with the 10 keV acceleration voltage. Figure adapted from Zehbe et al., 2010.

It is also possible to distinguish cells from biomaterials even easier than it was previously described, for example by exposing samples to osmium tetroxide. Osmium tetroxide has been used for resolving neural projections and blood vessels from polyimide scaffolds (Watlinga et al., 2010) and for studying general cell proliferation in polypropylene scaffolds (Dorsey et al., 2009). In more complex samples, like in tissues, there could still be unexploited, fairly easy ways to enhance the specificity of the semi-specific stains. For example, in conventional histology it is possible to purposely restrict the binding of monovalent Ag cations (Ag$^+$) and make them to bind only in specific types of tissues. By keeping metallic copper in contact with staining solution during the so called Bodian's staining, one can enhance the SNR arising from neurofibrils, axons and neurofibrally tangles of neural cells. That is because the copper ions compete from the same chelation places

found in connective tissues, why the reducible $Ag^+$ binds solely into the neural structures. (Kondo et al., 1996) Though, there is no marks so far that these kind of innovative ways are exploited in µCT imaging.

Like stated earlier, the benefit of the semi-specific stains is the much cheaper and simpler usage than it is with the specific labels. However, the risk of false positive signals might be higher in semi-specific contrasting agents as they lack the utilization of highly specific intermolecular interactions. For example, even though the negatively charged GAGs are abundant in certain tissues, the use of solely charge dependent contrasting could result signals which do not only include stain interactions with the GAGs, but also the interactions with the other types of negatively charged structures. Thus, for avoiding false results, care must be taken and comprehensive control experiments are important to design with semi-specific contrasting methods like always.

## 2.2.4. Specific labeling

Usually, specific contrasting agents are transported into samples in their low density states. For example, in the case of the specific Ag labeling the contrasting mechanism is usually based on the reduction of $Ag^+$ ions into metallic Ag colloids under the peroxidase activity, like horseradish peroxidase (HRP). $Ag^+$ ions are usually provided by the commercial Ag generation kits. For example, the EnzMet$^{TM}$ for General Research Applications kit can be used for generating localized silver under the peroxidase activity (EnzMet™ 6010 Manual). Antigen targeted primary antibodies are usually transferred first into the sample and the enzyme conjugated secondary antibodies recognize them. (Metscher & Muller, 2011; Chien et al., 2013) This kind of approach resembles a lot of the specific stains made in conventional histology, where the part of the signal amplification is done by binding multiple secondary antibodies to singular primary antibodies (Bancroft & Gamble, 2008).

For making specific µCT examinations, it could be possible to enhance directly the already present metal particles, conjugated directly to the primary antibodies (Chu et al., 2005). However, it seems like this more straightforward method is not yet utilized for the µCT imaging. Instead, antibodies

conjugated directly to Au nanoparticles are already applied for tracking intravenously lymphocytic cluster of differentiation 4 (CD4) surface receptors in mice, with no post-amplification steps at all (figure 12; Eck et al., 2010). Thus, if the target antigen is abundant and easily accessible, no signal enhancements are needed for distinguishing the target from the other parts of the studied sample. At least the easy access is guaranteed if the epithelial surface antigens are studied intravenously.

In addition to specific intravenous contrasting, histological samples can also be stained by specific techniques. In enough small and permeable samples the staining might be successful by modest efforts (figure 13). However, the $Ag^+$ ion diffusion is not the major bottle neck for the reach of the specific contrasting. The used antibodies and their conjugates are much more spacious than the $Ag^+$ ions, which sets big challenges for the uniformity of the specific contrasting. Samples having strong and dense extracellular matrix (EMC) could be unmasked, like by using enzymatic digestion, a well-known method in the conventional histology (Bancroft & Gamble, 2008). Enzymatic digestion based unmasking techniques could also be used for preparing µCT samples, as it removes diffusion obstacles for externally applied contrasting agents. So far it seems like there is no literature available about benefiting this technique for µCT contrasting purposes.

Small animals and histological pieces are certainly not the only types of samples which can be studied by the specific contrasting. Cultured cells on supportive materials, like on biopolymer scaffolds or cell culture medium, can also be stained by the stepwise manner with antibodies (Chien et al., 2013; Thimm et al., 2012). Antibody conjugated HRP enzymes are not only capable for reducing cationic $Ag^+$ to dense colloids, but they can also be used for making nickel enhanced 3,3'-diaminobentidin stains (Chien et al., 2013). Furthermore, enzymatic reactions are not necessarily needed at all for generating specific contrasting signals, which was the case also with the specific intravenous stains done in mice (figure 12; Eck et al., 2010). Even relatively large FeO particles, 0.5-1.5 µm in diameter, can be specifically adsorbed onto target surface-antigens, presented by the cells seeded into porous scaffolds made of biomaterials (figure 14). First, biotinylated antibodies are used for recognizing their target antigens. After washing the excess, unattached antibodies away, samples are treated by the solution containing streptavidin functionalized FeO particles. These particles form sandwich structures with the previously applied antibodies, further leading to local density enhancement of the target antigens. (Thimm et al., 2012)

Thus, in non-confluent biomaterial-cell hybrid samples the accessibility of even large contrasting agents is not an issue, because all the steps can be made by flow-through manner.
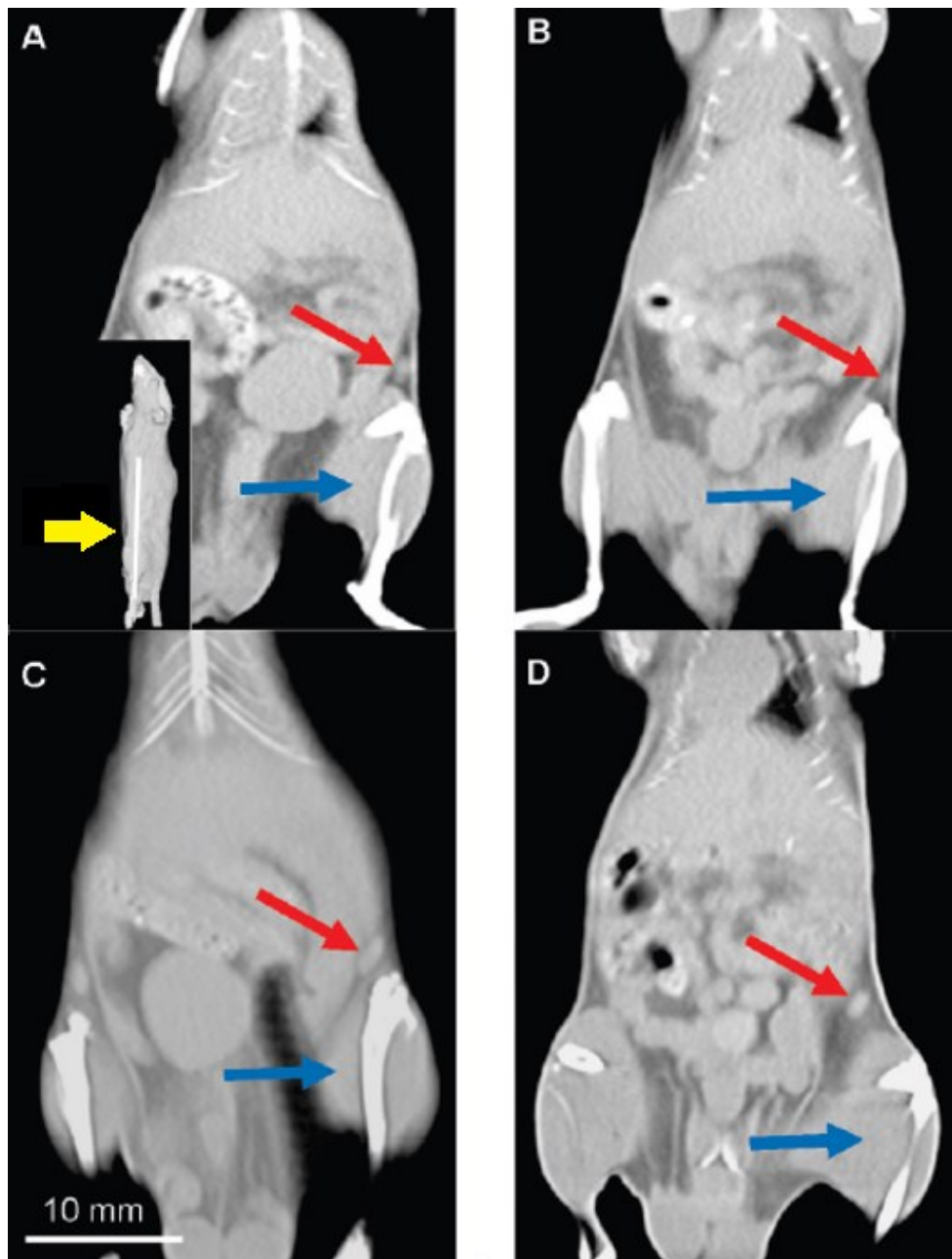


**Figure 12.** µCT images from mice before (A, B) and 1 h after the injection of Au nanoparticles (38 nm in diameter) conjugated to unspecific immunoglobulin G (IgG; C) and anti-CD4 IgG (D). The smaller figure in A shows the orientation of the cross-section plane (white bar, pointed by the yellow arrow) of the larger µCT images. The white arrow points along the viewing direction. The targeted nanoparticles, conjugated with CD4 IgG antibodies, show some contrast enhancement of inguinal lymph nodes (red arrows in B and D), whereas virtually no change in signal intensity is visible for the nonspecific controls (red arrows in A and C) according to the article (Eck et al., 2010). For the better comparability of the X-ray densities, the hind limb muscles have been set as a standard brightness value (blue arrows). The better target enhancement in the BD image pair is more obvious when the Hounsfield units of different images are compared. The average measured X-ray densities of the individual lymph nodes (red arrows) in Hounsfield units are 47 (A), 26 (B), 52 (C) and 121 (D). Thus, the density changes are 5 and 95 units for the AC and BD image pairs respectively. The spatial resolution is 15 µm and the 2D images were acquired by using polychromatic tube radiation with the 80 kV acceleration voltage. Figure adapted from Eck et al., 2010.
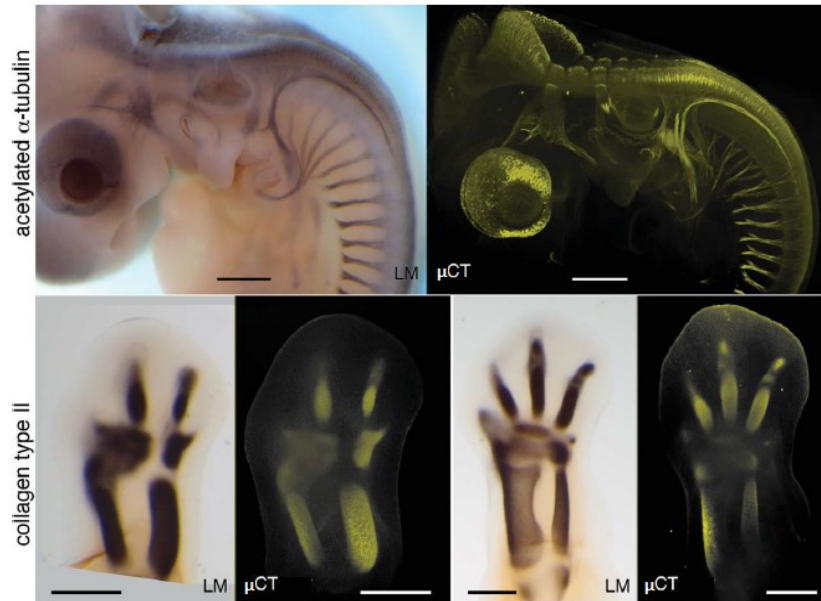
**Figure 13.** Comparison of light microscope (LM) and μCT images from the same antibody stained embryonic chicks. In the LM images, the generated Ag colloids can be seen as dark grey areas, because the Ag particles scatter and absorb visible light. In the reconstructed μCT images, the brighter and greener the color is, the denser the corresponding area is. In the upper row, acetylated α-tubulin primary antibodies are used for localizing HRP conjugated secondary antibodies and Ag colloids near the antigens. The same thing is done also in the lower row images, but the primary antibody is changed to one recognizing the type II collagen antigens. Acetylated α-tubulins and type II collagens are intracellular and extracellular antigens respectively. As it can be seen from the images, the signals captured by the LM and μCT overlap quite well. In these kind of modestly transparent samples, the Ag signals can be seen with the LM, but the 3D signal distributions cannot be resolved by this method. Furthermore, in the thickest parts of the sample it is hard to clearly see inside the sample without μCT. The spatial resolution in the μCT images is 5 μm and the 2D images were acquired by using polychromatic tube radiation with the 25 kV acceleration voltage. All scale bars are 500 μm. Figure cited from Metscher & Muller, 2011.
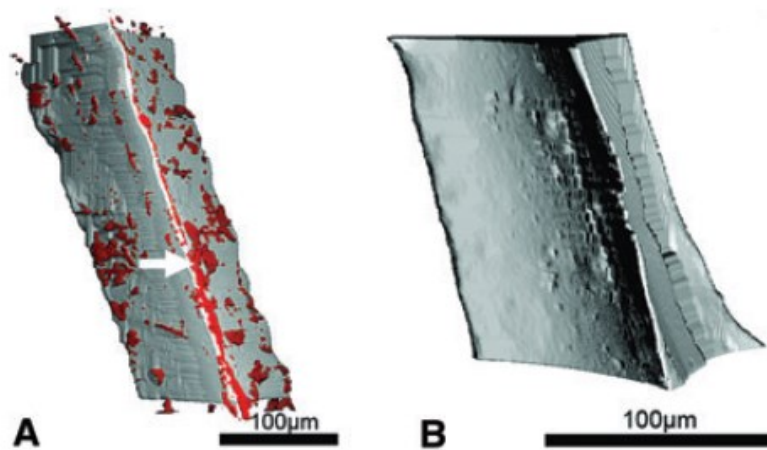


**Figure 14.** Human dermal microvascular endothelial cells cultured on polyurethane scaffolds (grey), labeled by using CD34 targeted FeO particles (red) and imaged by μCT (A). The sample B is a labeled control without the cultured cells. A threshold level for attenuation intensity was used for distinguishing dense FeO particles from the lighter biomaterial. Voxels exceeding this intensity level are shown in red and pointed also by the white arrow. As it can be seen from the sample B, the FeO particles do not have adsorption affinity against the scaffold without the antigens provided by the cells. The estimated spatial resolution is 6 μm and the 2D images were acquired by using monochromatic synchrotron radiation with the 40 keV acceleration voltage. Figure adapted from Thimm et al., 2012.

## 2.2.4.1. Common steps and technical details for specific contrasting

Like described earlier, specific labeling can be used in many ways and applied on many types of samples. Many steps and technical details of the specific contrasting are common with the conventional histology, especially if the two staged HRP functionalized antibody based Ag labeling approach is used. In the following sections, these steps and details are discussed in general level. These specific Ag contrasting can be divided into 7 main steps, described in the figure 15.
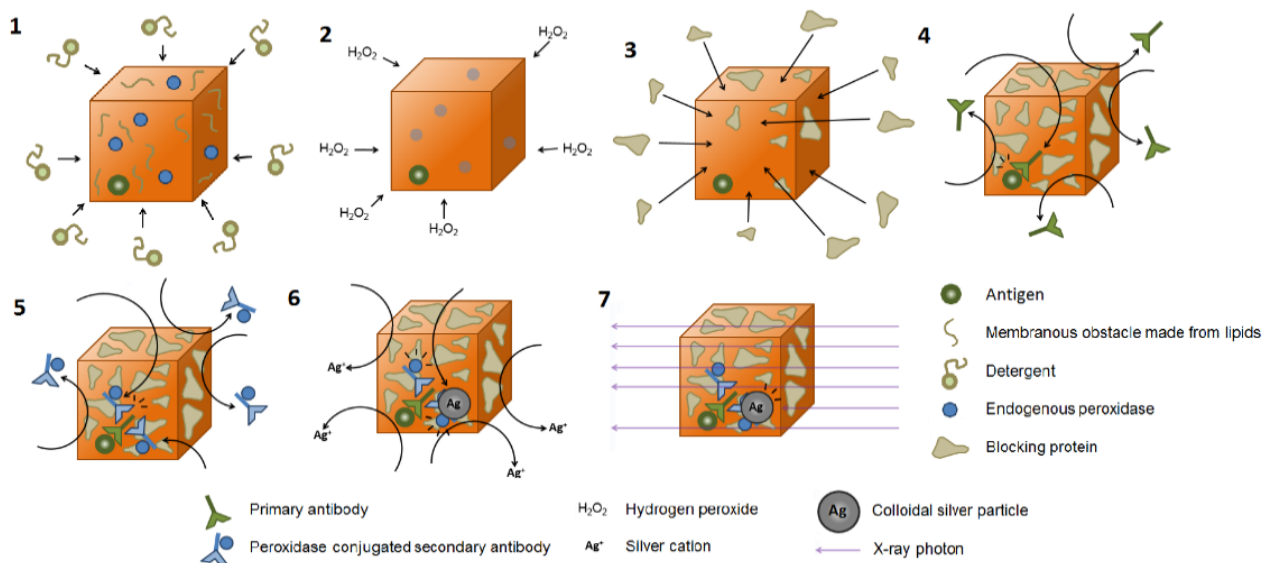


**Figure 15.** The usual steps used for making specific, two staged HRP functionalized antibody Ag contrasting. 1. After the fixation, membranous obstacles, made from lipids, are removed and/or permeabilized by the detergents. 2. Endogenous peroxidases are inactivated by the $H_2O_2$ treatment. 3. Possible non-specific binding sites for proteins are saturated by adding blocking proteins, so that unwitting interactions with coming antibodies do not occur. 4. The target antigen is recognized by the primary antibody and excess, unbound antibodies are washed away afterwards. 5. Singular primary antibodies are recognized by multiple, HRP functionalized secondary antibodies and excess, unbound antibodies are washed away afterwards. 6. $Ag^+$ is reduced to localized colloids by the imported, HRP activity. 7. 2D μCT images are acquired. The X-ray attenuation is enhanced near the target antigens because the now present dense Ag colloids.

Many common buffers can be used as carrying solutions during specific labeling, like PBS, Tris buffered saline (TBS) or maleic acid buffer with NaCl (Chien et al., 2013; Thimm et al., 2012; Metscher & Muller, 2011), which is the case also in conventional histology (Bancroft & Gamble, 2008). The used carrying solution should be chosen according to technical datasheets provided by the manufacturers of staining agents, and/or possibly already made research focused on the similar types of samples. Usually, buffers with physiological pH are used with antibodies, because pH around 7.4 keeps the antibodies in somewhat isoelectric state,

enhancing their immunoreactivity and solubility. Since alkaline phosphatases are not used in the specific contrasting, there is no clear reason to favor either PBS or TBS over each other. (Buchwalow & Böcker, 2010) On the other hand, usually, during the lasts step of the staining, phosphates and other salts are washed away by the ddH$_2$O for avoiding the precipitation of the Ag$^+$ salts (EnzMet™ 6010 Manual).

Like in the conventional histology, samples are first fixed prior to other staining steps, for example by formaldehyde or glyoxal based fixatives (Chien et al., 2013; Thimm et al., 2012; Metscher & Muller, 2011). Alcohol based dehydrating solutions may also be used as fixatives for precipitating and coagulating proteins. Formaldehyde is usually still used with the alcohol for linking the proximate biomolecules together. The use of alcohol could aid the staining procedures especially with large, lipid containing samples, by helping extracting lipids. Thus, alcohols could also be thought as permeabilizing agent. (Bancroft & Gamble, 2008) It is also possible to perform the sample permeabilization in a separate step (figure 15 step 1), which is more common case during examining cultured cells. Permeabilization can be done with the general detergents like Triton X-100 and/or saponin for example (Chien et al., 2013; Metscher & Muller, 2011). For eliminating false positive signals arising from the endogenous peroxidases, samples can be treated by 0.1% to 3% hydrogen peroxide solutions before or after the permeabilization (Chien et al., 2013; Metscher & Muller, 2011; Bancroft & Gamble, 2008), for forcing the enzymes to commit suicide reactions (figure 15 step 2; Frey & Hegeman, 2007).

Like any protein, antibodies can bind unspecifically into samples by strong and unwitting hydrophobic, hydrophilic and/or ionic interactions. This could lead to false positive signals arising from the locations where the target antigens are not present. Like in the conventional histology, samples are usually blocked by sacrificing inactive proteins for filling the unspecific binding sites before the antibodies are applied (figure 15 step 3). The blocking solutions can be homogeneous like BSA dissolved in buffer (Chien et al., 2013), but heterogeneous mixtures like serums and commercial blocking mixes can also be used (Metscher & Muller, 2011). Heterogeneous blocking solutions may give more comprehensive blocking results than the homogeneous ones, but any blocking solution should not contain homologous structures to the studied epitopes and used primary antibodies so that the blocking components are not recognized by the antibodies. Furthermore, the chosen primary antibodies should not be produced in the same species where the

sample is originated from, for minimizing the risk of secondary antibody recognizing the endogenous antibodies and their homologous structures in the sample. (Bancroft & Gamble, 2008)

The correct antibody dilutions should be tested by titration and staining known samples which contain the target antigens. For example, without correct dilutions false negative results could occur if an antigen rich sample distributes the low amount of used primary antibodies so much that the antibodies are not concentrated enough for producing strong localized signals. Furthermore, because there is a certain probability for antibodies to bind unspecifically into the sample in any case, too high antibody concentrations may lead to false positive signals. After the antibodies are applied (figure 15 steps 4 and 5), it is important to wash the unbound ones away, so that unwitting primary-secondary antibody complexes are not formed and the excess secondary antibodies do not produce unwitting signals. Commonly, the carrying buffer itself, without the antibodies, is used as washing solution so that the change in chemical circumstances do not unwittingly initiate the antibody precipitation. As a small but important technical detail, it is important to avoid the solvent evaporation during the antibody labeling, so that the buffer do not concentrate and further lead to salting out effect. (Bancroft & Gamble, 2008)

After the excess secondary antibodies are washed away, the Ag generation/enhancement procedures can be performed (figure 15 step 6). For example, if the commercial EnzMet Ag generation kit is used for producing localized colloidal silver around the imported peroxidases, after the carrying buffer is changed to $ddH_2O$, only three reagent solutions are needed to add in stepwise manner for generating the signal (EnzMet™ 6010 Manual). If more intense signal is required, the formed colloid could be further amplified by using enhancement kits, like the Silver Enhancement Kit produced by Sigma-Aldrich (Sigma-Aldrich SE100 Manual). After appropriate signal strength is acquired, samples can be simply imaged by μCT.

# 3. Aims of the study

This study had three main aims. One of them was to test the feasibility of the three common background stains for examining overall anatomy of adult zebra fish samples with μCT. Different forms of IKI, I2E and PTA contrasting methods were tested. The contrasting protocols were iteratively optimized until satisfactory results were acquired with each stain; comprehensive diffusion of the contrast agents and clear distinctiveness between anatomical structures were acquired. Second aim was to apply I2E staining further for finding the proof of concept for examining fine structural dissimilarities between the dystrophic Royal College Surgeons (RCS) rat retinas and control retinas. Third main aim was to show that the used X-ray tube source based μCT device and the antibody guided Ag precipitation method together can be used for examining subcellular structures of adipose stem cells (ASC).

# 4. Materials and methods

In this section, after the used µCT device and reconstruction software are described, the used *materials and methods* for reaching the three main aims are described. The *Materials and methods* of the each main aim are divided into necessary sub-sections, and their results are discussed in the corresponding order in the *Results and discussion* section.

## 4.1. Used µCT Device and Reconstruction Software

All the imaging data were acquired by the MicroXCT-400 device (Xradia) and the imaging data were reconstructed by the Xradia's own XMReconstructor Cone Beam (8.1.6599) and possibly further processed by the Avizo Fire (8.0.1) 3D analysis software.

## 4.2. Comparison of IKI, I2E and PTA in zebra fish imaging

### 4.2.1. Preparing background contrasting solutions

I2E staining solution was made by diluting 1% w/v solid $I_2$ (207772, Sigma Aldrich) into absolute ethanol. The commercial IKI solution (3.7g/l $I_2$ and 7.4 g/l KI in water, Lugol's solution, 62650, Sigma Aldrich) was used as such and by diluting it by 1:10 with $ddH_2O$ only or with 10X PBS for having physiological solution. PTA (P4006, Sigma Aldrich) was diluted to concentrations 0.3-4% w/v with 50% or 70% ethanol-$ddH_2O$ solutions. PTA treatment was tested with and without 10 mM Tris buffer, which was titrated to pH 7.5 with 10 mM NaOH. During the titration, the PTA solutions might became cloudy and was re-clarified by heating the container with hot tap water for 10 min. The pH of the non-buffered PTA was between 1-3, depending on the amount of the PTA. PTA solutions were also supplemented with and without 0.1 % Triton X-100 (T8787, Sigma Aldrich) and Saponin (47036, Sigma Aldrich).

## 4.2.2. Experimental iteration of zebra fish contrasting

Development of the contrast agent enhanced µCT imaging procedure of the zebra fish comprised of multiple sub-series, in which the different contrasting parameters were adjusted. The consecutive sub-series were always designed according to the previous results. Every sample in the same sub-series was treated like the parallel co-samples, only one of the studied parameters was varied at a time. This iterative process was continued until satisfactory contrasting results were reached. Possible cross-reactions between the used substances were studied in test tube experiments before the solutions were applied on the histological samples.

Zebra fish samples were provided by the Zebrafish facility in BioMediTech (professor Mika Rämet, University of Tampere). The tails and heads of the previously scarified fish were first removed with a scalpel for aiding the diffusion of the contrasting agents. The fish were fixed in NBF, either with or without 0.1 % Triton X-100 permeabilization. Because the size of the fish varied moderately, it was estimated that the samples were fully saturated by the fixative if the samples were fixed for at least 24 h. After the fixation, the samples were washed in the corresponding carrying solution of the coming staining solutions, excluding some of the PTA treatments in which the washing solutions included saline, not used during the contrasting phase. The samples were washed 2 times for 1 h, and in some of the PTA stains kept in the fresh washing solution for 1 to 2 extra days. All the samples being I2E treated were washed with the PBS after the fixation and dehydrated into absolute ethanol by rocking the samples overnight in 70%, then 2 h in 95% and finally 3 h in absolute ethanol. After washing, samples were put in the contrasting solutions and kept there for varying amount of time, from overnight to 8 days.

After the contrasting, IKI samples were quickly rinsed and washed 2 times for 30 min in ddH$_2$O or PBS, I2E samples in absolute ethanol and the PTA samples in the corresponding carrying solution with or without modifications. After PTA treatments, samples were washed either by the solution in which the PTA was replaced by the saline, only the corresponding ethanol solution were used or pure ddH$_2$O was applied. The unstained control fish was imaged after the fixation with NBF and washing in PBS. All the treatments were made in 4°C, excluding the PTA stains which were made in room temperature (RT) for avoiding the precipitation.

### 4.2.3. Zebra fish μCT imaging

Zebra fish samples were placed in plastic tubes with their corresponding fresh washing solutions. Before the imaging, samples were mechanically and thermally stabilized in RT for at least 5 hours. μCT imaging was performed by using non-filtered X-ray radiation, produced by 80 kV acceleration voltage and 10 W source power. 1600 projections were evenly acquired from the whole 360° with 3-5 s exposure time per projection. 1X objective was used which gave voxel size of approximately 20 μm. Possible contrast agent diffusion out of the sample was followed from the so called drift file, a pack of images collected from a fixed angle during the whole μCT imaging.

# 4.3. Pathogenesis of dystrophy in rat eyes – Examination with I2E

## 4.3.1. I2E contrasting of rat eyes

The I2E staining was chosen for the rat eyes. It was considered to be the safest choice for preserving the fragile retinal morphology. That is because during the I2E staining the samples are transferred into the absolute ethanol by the stepwise manner, which is the case also with the conventional histology, before the samples are embedded into paraffin blocks (Bancroft & Gamble, 2008). And if compared with the relatively large and charged PTA complexes, faster penetration was assumed for smaller and hydrophobic $I_2$ molecules.

3 control and 3 dystrophic adult RCS rat eyes were provided by the Ophthalmology Group in BioMediTech (group leader adjunct professor Heli Skottman, University of Tampere). The eyes were put in cooled PBS and rinsed a couple of times. Mild Davidson's fixative was prepared by making 33% ethanol, 10% glacial acetic, 0.74% formaldehyde solution. The eyes were immersed in the fixative overnight. The eyes were then rinsed and washed with 70% ethanol for 30 min and kept in fresh solution overnight. During the next day, the eyes were rinsed and kept in 95% ethanol overnight. Then the eyes were rinsed and kept in absolute ethanol for 4 hours and finally transferred into the I2E solution, made by diluting 1% w/v of $I_2$ (207772, Sigma Aldrich) with absolute ethanol. All eyes were kept in the I2E solution for over 3 weeks to ensure the chemical stability of the samples. Every treatment were made in 4 °C and with gentle rocking, excluding the 3 week stabilization which was performed in static conditions.

## 4.3.2. Rat eye µCT imaging

The eyes were transferred into sample holders made from 2 ml plastic syringes. The sample holders were filled with the same I2E solution used in the contrasting in order to preserve the chemical circumstances. This also eliminated the outward diffusion of the contrasting agent, the issue seen during the previous zebra fish experiments. The eyes were positioned so that the axis of rotation was parallel with and went close the axis between the nerve bundle and the center of the cornea. It was known from an earlier trial imaging that the $I_2$ highly concentrates into the lens which makes it dense. By positioning the eyes like described, greater amounts of X-ray photons passed through the retina, which made easier to collect enough information from the eyes by tolerable imaging times.

Before the imaging, samples were mechanically and thermally stabilized in the sample holders in RT for at least 5 hours. µCT imaging was performed by using non-filtered radiation, produced by 75 kV acceleration voltage and 10 W source power. 1600 projections were equally acquired from the whole 360° with the 100 s exposure time. 4X objective was used for gaining 3 µm voxel size and the whole eyes were captured into FOV.

## 4.4. Specific actin and lamin contrasting of ASC samples

### 4.4.1. ASC Culturing

ASC were received from our collaboration partners at the Adult Stem Cell research group in BioMediTech (Group leader adjunct professor Susanna Miettinen, University of Tampere). The 100 ml lots of 5% HSPaa + P/S cell culturing medium were prepared by mixing together 93 ml DMEM/F-12 (Gibco supplements, Life Technologies); 5 ml HSPaa (Paa Laboratories); 1 ml GlutaMAX (Gibco supplements, Life Technologies) and 1 ml of P/S-solution consisting of 100

U/mL penicillin and 0.1 mg/mL streptomycin (BioWhittaker reagents, Lonza). Polystyrene 24-well cell culturing plates (Nunclon, Nunc) were used for the culturing. Approximately 1000 ASC were applied into each well from the earlier cultures in the mentioned culturing mediums. Earlier cultures were harvested by 1% trypsinization (TrypLE, Lifetechnologies) in PBS for 5-10 min in 37 °C, after the previous culturing mediums were washed away with PBS. Trypsin was neutralized by pipetting plenty of culturing medium onto the trypsinized cells, which saturates the trypsin by the abundance of its substrates. Detached cells were removed with the medium by pipetting, pelleted by gentle centrifuging in 1500 rpm for 5 min and were finally resuspended back into the fresh culturing medium. Cells were grown in 37 °C and 5 % $CO_2$ in a cell incubator for 3-14 days for reaching suitable cell density with many individual isolated cells.

## 4.4.2. Anti-β-actin and anti-lamin labeling

After the ASC were cultured, all the contrast labeling steps were made in RT. The culturing medium was removed and the samples were rinsed and washed 3 times for 4 min in PBS with gentle rocking. Cells were fixed either with 4% formaldehyde in PBS solution or Davidson's fixative. The latter fixative consisted of 33% ethanol, 10% glacial acetic and 8% formaldehyde. The Davidson's fixative was trialed for two reasons; for observing its possible effects on the cell morphology and for testing if ethanol based fixation could enhance staining by permeabilizing the possibly three dimensionally more confluent samples in the future. All the fixations lasted for 10 min and the samples were washed afterwards as described previously.

The samples were permeabilized with 0.1 % Triton X-100 in PBS for 10 min. After the permeabilization the samples were washed with PBS like earlier. Endogenous peroxidases were not inactivated because earlier experiments revealed that the used cells did not have visible endogenous peroxidase activity. The 1 hour unspecific binding site blocking was performed by using either 4% w/v BSA in PBS or ready-to-use normal horse serum solution. The horse serum was included in the histological immunodetection kit (ImmPress Reagent, Vector Laboratories) with the HRP-conjugated Anti-Mouse antibody (the functionalized secondary antibody) used later for the

primary antibody detection. The parallel BSA blocking was investigated for future labeling methods which could exploit other technologies than the ImmPress antibodies.

After the blocking, the primary antibodies were applied in 0.5% w/v BSA in PBS carrying solutions, directly after the blocking solutions were removed. Anti-actin (against β-actins, SC-47778, Cruz Biotechnology) and anti-lamin (against A + C lamins, 131C3, Abcam) antibodies were diluted in the carrying solution by 1:100 and 1:200, respectively. The primary antibodies were let to bind for 1 hour. After the binding, the excess primary antibodies were washed away with PBS like earlier. The ready-to-use HRP-conjugated secondary antibody was used as such for detecting the previously applied mouse hosted primary antibodies. Secondary binding lasted 1 hour and the excess antibodies were washed away with PBS like earlier. The samples were next rinsed and washed 3 times for 4 min with ddH$_2$O. Finally, colloidal Ag particles were generated by the peroxidase dependent silver reduction reagents (EnzMet for General Research Applications, Nanoprobes). ddH$_2$O was removed from the sample wells and the equal volumes of kit reagents A, B and C were added stepwise at 4 min intervals. The whole procedure was performed in low light conditions for avoiding the photoactivated background Ag reduction. The reagent C initiates the Ag reduction which was continued for 1-5 min, for reducing specific Ag as much as possible without having much background. The formation of background Ag was followed from the parallel non-antibody-treated control samples and with microscope. For seeing the non-specific binding of the secondary antibody, control samples without the primary antibodies were also stained in parallel with the other samples. The control samples were treated like others but the primary antibody containing solutions were replaced with pure corresponding carrying solutions. The Ag reductions were stopped by rinsing the samples multiple times with excess amounts of ddH$_2$O.

### 4.4.3. Parallel fluorescence DAPI and phalloidin stains

After the Ag signals were generated, parallel fluorescence staining were performed for examining the co-localization of different probes having similar targets. Phalloidin (Alexa Fluor 488, A12379,

Life Technologies) and 4',6-diamidino-2-phenylindole (DAPI; #4083, Cell Signaling Technology) fluorophores were used in parallel with the anti-actin and anti-lamin antibodies respectively.

Phalloidin stock solution was prepared by diluting the lyophilized vial content into 1.5 ml methanol in low light conditions, for reaching the 6.6 µM stock concentration. The phalloidin stock solution was stored in dark -20 °C, until the staining solution was made by diluting the stock by 1:40 in 0.5% w/v BSA in PBS. The phalloidin stained samples were first rinsed and rocked gently in 0.5% w/v BSA in PBS for 1 h for restoring the physiological circumstances and for re-blocking the possible unspecific protein binding sites. After the samples were stabilized, the pure carrying solution was changed to the staining solution and the samples were gently rocked in dark for 30 min in RT. After the stain, samples were rinsed and washed 4 times with PBS for 5 min. The samples were protected from light until the fluorescence microscope analysis was made.

DAPI stock solution was also prepared in low light conditions by dissolving the lyophilized DAPI into ddH$_2$O. The stock concentration was 1 mg/ml. Anti-lamin stained cells were kept in ddH$_2$O because DAPI is suitable to be used in ddH$_2$O and there was no need to perform blocking prior to the non-protein label. Previous ddH$_2$O was removed from the samples and replaced by 1:1000 DAPI stock dilution made in ddH$_2$O. Samples were stained in dark for 4 min with gentle rocking in RT. After the staining, samples were rinsed multiple times and washed 4 times for 5 min with ddH$_2$O for removing the excess DAPI. Samples were kept in dark until examining them with the fluorescence microscope was made.

## 4.4.4. Final ASC sample preparation and µCT imaging

After the well plates were examined with light and fluorescence microscopes, a punch was used for severing the bottoms pieces out of the wells. First, a piece of cardboard and tissue papers were piled over each other for making a suitable, soft surface. The lid was removed from the well plate and the wells were covered by parafilm for keeping the liquids in the wells during the punching. Only the prepared well was uncovered by a scalpel, and the tip of the punch was gently placed on the bottom

in ddH$_2$O. A hammer was used so that the operated bottom broke along the edge rim, as the soft surface bended underneath the tip of the punch. Because the liquid in the well escaped after the punching, the detached bottom pieces were quickly transferred into fresh ddH$_2$O by tweezers. The cellularity of the sample pieces was confirmed by a microscope. A plastic tube, about 16 mm in diameter, was filled by ddH$_2$O in which the sample pieces were placed. Samples were supported by other suitable pieces of plastic and foam, the cap was sealed. Finally, the whole setup was knocked gently multiple times for releasing possible tensions which could later cause sample movement during the imaging.

µCT imaging was performed by using non-filtered radiation, produced by 40 kV acceleration voltage and 10 W source power. 1600 projections were equally acquired from the whole 360° with the 65 s exposure time. 10X objective was used for gaining the spatial resolution of approximately 1 µm.

# 5. Results and discussion

## 5.1. Outcomes of background contrasting in zebra fish

In the control female zebra fish, only the bones, scales and mineral rich food inside intestines were enough dense to be visible in the μCT images (figure 16 and 17). If the image histogram was adjusted correctly, the weak internal parts was seen as dense as the surrounding medium, while some less dense cavities were also found. For example the kidney, lying right under the spine, was recognized by this lesser dense tone. These negligible structures are not shown in the figure 16, as the histogram of the control fish was adjusted by the same principles with the stained samples.

All of the optimized background stains greatly enhanced the soft tissues of the fish (figure 16 and 17). Generally the contrast enhancement of soft tissues did not vary much between the stains. Only with the IKI stain some fatty-like tissues were seen all around the fish, while the visibility of bones and scales decreased, as discussed more in the following sections. All of the contrasting agents started to diffuse out of the samples after the contrasting, why the samples were imaged right after the final washes. It was concluded that the outward diffusion had negligible contribution in the imaging accuracy in the acquired resolution. In the PTA stained fish the outward diffusion was decreased a little by applying post-saline, discussed more in the corresponding sub-section.

### 5.1.1. I2E contrasting results of zebra fish

2 day I2E staining gave directly good results with no need for optimization. Thus, the used staining procedure did not fundamentally differ from the I2E protocol Brian Metscher used for staining chick embryos (figure 9; Metscher, 2009). The penetration of the stain was fastest from the three tested and the contrast enhancement was comprehensive. Multiple different tissues and organs were distinguishable by the varying absorption intensities and sharp feature interfaces (figure 16 and 17). Some deformations were seen in the fish anatomy, like the detachment of the swim bladder. Furthermore, in some cases the back of the fish seemed to be slightly wrinkled inward, which was
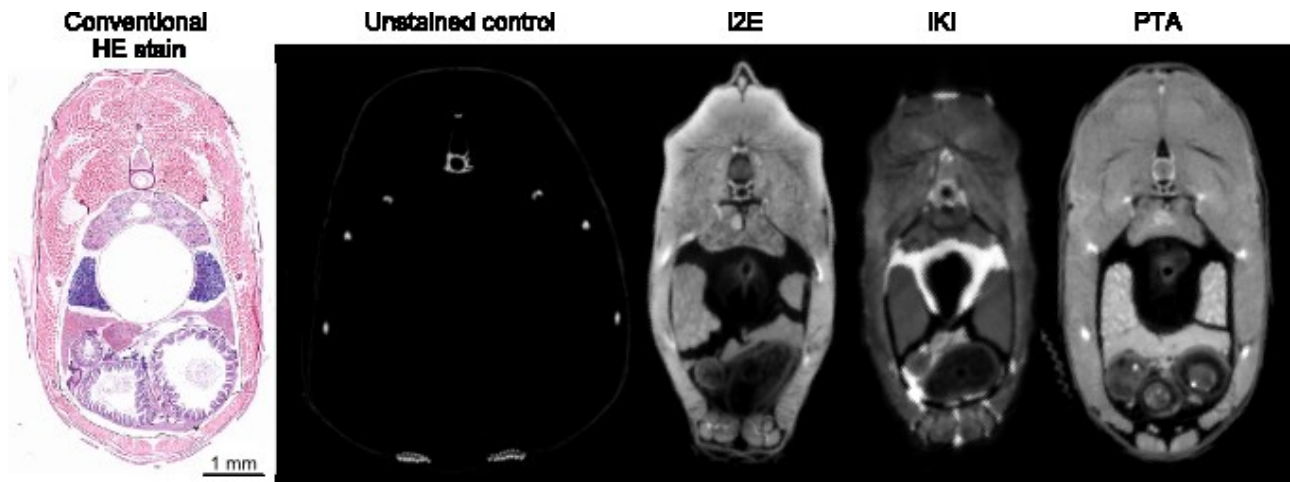
**Figure 16.** Light microscopy image of a hematoxylin and eosin (HE) stained zebra fish in paraffin slice (left) and the virtual cross-section from the μCT imaged zebra fish (right with the black background, spatial resolution approximately 20 μm). In the μCT images, the denser areas are shown with the brighter color. The histograms of the μCT images were adjusted by increasing the dark minimum input until the background signals vanished. The maximum inputs were brought so low that the lower intensity features were enhanced, but the high intensity features did not much saturate and spread over the softer areas. The image of the IKI fish shown here is slightly blurry because the unwitting sample movement during the imaging. The image of the HE stained paraffin slice was adapted from the Ven & Wester, 2014.
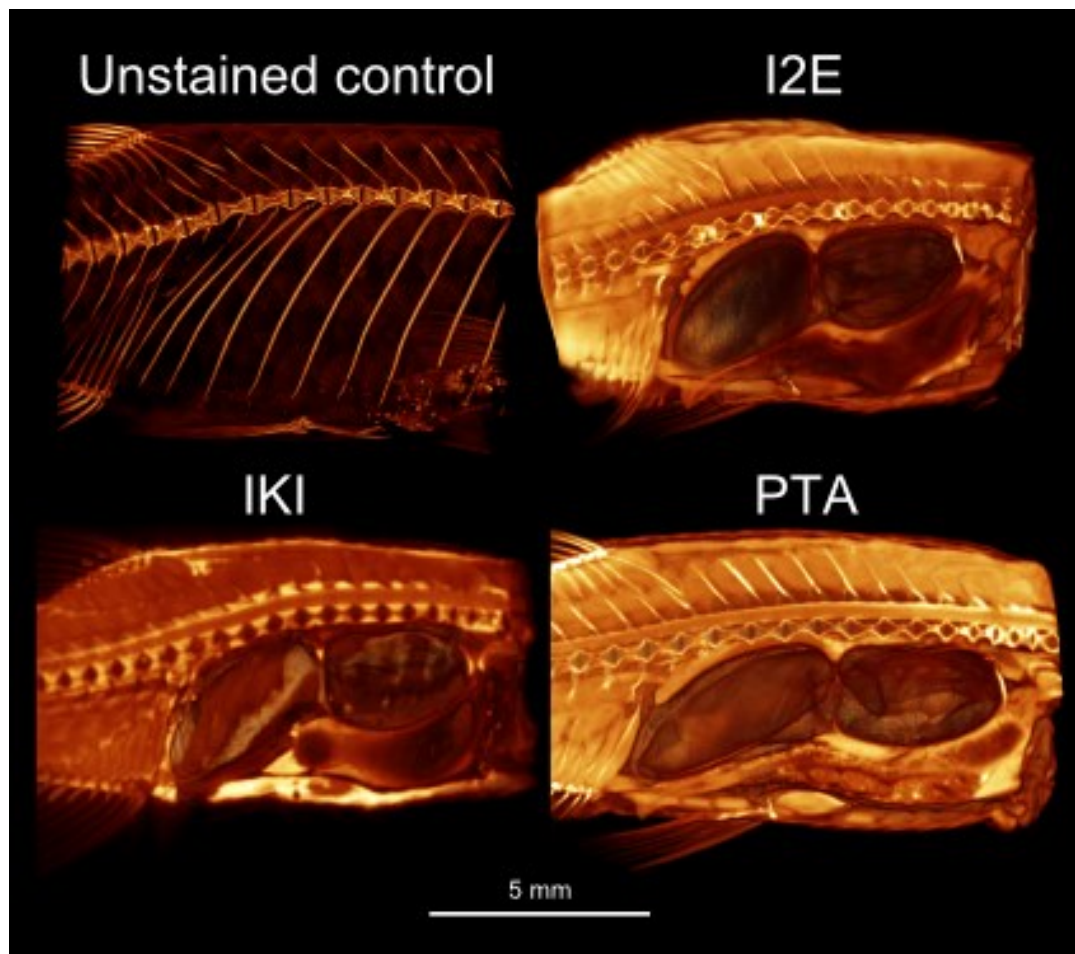


**Figure 17.** Virtual 3D renderings and their lengthwise cross-sections from the μCT imaged zebra fish. The denser areas are brighter and more opaque, while the lesser dense areas are more dim and transparent. The histograms were the same as in the figure 16. The spatial resolution in the μCT images is approximately 20 μm.

45

possibly due to the presence of $I_2$ and/or ethanol dehydration. Empty cavities, surrounding the entrails, could also be seen. These cavities were possibly due the shrinkage of the tissues and/or dissolution of fatty tissues in ethanol, leaving empty spaces behind. Still, the fish anatomy was preserved at least as well as in a typical cross-sectional paraffin slice made by conventional histological methods (figure 16).

Fixation with detergents did not have any visible effect on the penetration of the I2E stain. In fact, permeabilization with the Triton X-100 could disturb the signal distributions. Triton X-100 molecules have unsaturated benzene rings which seemed to become halogenated by the presence of $I_2$, which led to increase in polarity by the inductive effect, and formed insoluble precipitates. This was noted in the preliminary test tube experiments as cloudiness and colloidalization when $I_2$ and Triton X-100 were mixed together, even in mild solutions.

## 5.1.2. IKI contrasting results of zebra fish

3 day staining in undiluted IKI solution gave the best and fastest results from all of the tested IKI protocols. Generally, the stain was as comprehensive as the other stains, but only the IKI stained fish showed interesting high density structures surrounding the entrails, spinal cord and lying beneath the skin (figure 17 and 16). The largest continuous structures were found around the duct connecting the two compartments of the swim bladder. Globular, high signal intensity anomalies were also seen in some of the IKI stained fish, usually diffused inside the cavity of the detached swim bladder. These structural anomalies were possibly originated from the surrounding fatty tissues, usually seen as more ordered structures aligned along the interfaces of the other structures. Metscher also noticed these high intensity structures in his IKI stained chick embryos (figure 9), but concluded that the signals originated from the trapped blood (Metscher, 2009). According the *Histology and Histopathology Atlas of the Zebrafish*, the tissue surrounding the duct between the two compartments of the swim bladder is mesenchymal tissue and it consist mainly from the adipose tissue (Ven & Wester, 2014). This, and the distributions right underneath the skin, highly suggest that the IKI stain is somewhat semi-specific contrasting agent against adipose tissues. The

staining mechanism is most likely due to covalent halogenation of the unsaturated lipid molecules (figure 8).

There are two possible explanations for the high intensity structures seen only in the IKI stained fish. With the ethanol based I2E and PTA staining solutions, the probable fatty tissues might simply become disturbed and dissolved away during the staining procedures. The second explanation is the presence of the KI salt in the IKI stain, which provides the small $I^-$ anions, not available in the other stains. It is possible that the high intensity structures are not only fatty in nature, but do also contain positively charged structures which suit well for chelating the supplied $I^-$ anions. However, the highly negatively charged, but much bigger PTA complexes did not seem to concentrate in the same locations like the IKI stain did, which implicates against the role of the charge. Thus, the halogenation reactions between the unsaturated fatty acids and the $I_2$ molecules have possibly the main contribution in the high signal intensity structures. The pure hydrophobic interactions between the fatty phases and unreacted $I_2$ molecules might also have contribution in the revealed features.

The IKI stain did not only enhance the overall contrast and the fatty tissues, but it also suppressed some of the features seen well in the other samples. In the IKI stained zebra fish, the bones and scales were not so easily distinguished from the softer tissues, as it was the case with the control sample and other stained fish (figure 16 and 17). Otherwise the overall signal intensity of the IKI stained fish did not remarkably differ from the other stains. Furthermore, the interfaces between the different structures were as sharp as they were in the I2E and PTA stained fish. The membrane of the swim bladder was detached and deformed also during the IKI procedure.

The 1:10 diluted IKI in ddH$_2$O did not work in our case, even though it was earlier reported that the final $I_2$ and KI concentrations of 0.1% and 0.2% w/v worked well with chick embryos (figure 9; Metscher, 2009). The Lugol's solution, or IKI, as a term does not universally describe an exact quantitative recipe for a solution, but describes what the solution do contain in. The commercial Lugol's solution used in this study had initially 0.37% w/v $I_2$ and 0.74% w/v KI concentrations, which were already in the same range with the solution Metscher used after the dilution he made (Metscher, 2009).

No differences in the staining results were seen if the samples were permeabilized with the Triton X-100 during the fixation, nor if the staining solutions were buffered with PBS. Though, like noted in the previous section about the I2E experiments, it would be wise not to use the Triton X-100 permeabilization in any case, because the unsaturated detergents might disturb the signal distribution by halogenating with the $I_2$.

## 5.1.3. PTA contrasting results of zebra fish

The biggest optimization difficulties were met with the PTA contrasting. If the earlier reported 0.3% w/v PTA in 70% ethanol was used (Metscher, 2009), the deepest penetration through the open muscle tissue in zebra fish was less than 1.7 mm during 8 days staining. The reach of the stain was even weaker through the impermeable skin of the zebra fish, evolved for aquatic habitats. Staining of the much smaller chick embryos, in which the deepest parts from the surfaces were approximately 500 µm away (figure 9), is feasible with the mentioned contrasting solution. Thus, it was obvious right from the beginning that the PTA contrasting procedure needed some fundamental adjustments to be applicable with the adult zebra fish samples.

The best PTA contrasting results were gained by staining the fish for one week in 1.2% w/v PTA dissolved in 50% ethanol with 10 mM Tris buffer which was titrated to pH 7.5 (figure 16 and 17). It was reasoned that by titrating the pH to physiological state, three different benefits could be acquired compared with the non-buffered PTA. First, because the non-buffered PTA solution had pH as low as 1.3, it is possibly not good for preserving the tissue morphology. Second, like described in the table 2, PTA complexes are in more disassembled state in the neutral pH than in the pH close to 1, $[PW_9O_{34}]^{9-}$ and $[PW_{12}O_{40}]^{3-}$ respectively. This state change likely decreases the overall size of the PTA complexes and speeds up the diffusion. Third, even though the PTA assemblies have higher negative net charges in the neutral pH (see above), it was thought to be worth trying if the neutralized stationary bases in the sample would lead to smaller hindering effect due to the decreased protonation. As it can be seen from the figures 16 and 17, together all the modified parameters gave successful PTA contrasting results.

In the successful PTA contrasting, the washing solutions were also supplied by the saline. The presence of saline seemed to have an important role for making good and comprehensive contrasting and for preserving the stain. First of all, during the test tube experiments, it was found that the PTA might become precipitated by the phosphates, especially in higher pH. Phosphates are abundant anions found in all living organisms, why their presence should be taken into account while designing PTA contrasting protocols. By the preliminary washing for over two days, the samples were let to stabilize in the saline based solution for replacing major part of the diffusive phosphates by NaCl. In the previously reported PTA staining of the chick embryos, the possibility of PTA precipitation with the endogenous phosphates was not considered at all, which might introduce contrasting anomalies in the examined samples (figure 9; Metscher, 2009). It was found that after the PTA contrasting that the isotonic circumstances also slightly helped for preserving the stain, while the outward PTA post-diffusion was fastest in the hypotonic solutions. This phenomena could be explained by the decreased electro-chemical gradient in the samples washed and imaged in the isotonic saline solution, as the large concentration differences would otherwise enhance the diffusion speed of salts. It was also thought that the isotonic circumstances could aid the preservation of the morphology of the samples, hence no wrinkling of the skin was seen in the PTA stained fish.

## 5.2. Retinal differences revealed by the I2E stain

It was obvious that without the staining or phase contrast imaging, the sophisticated morphology of the rat retina was impossible to see from the unstained eyes (figure 18). After the I2E contrasting, wide variety of structures and intensity tones were seen in the eyes as the $I_2$ was heterogeneously distributed in the samples. The most intensively stained part was the lens. High absorbance of the lens was known from preliminary trials and it was taken into account by positioning the eyes in this study as described earlier in the *Rat eye μCT imaging*. Other parts of the eyes were well visible as well, excluding the vitreous humour which was as dense as the surrounding I2E solution.
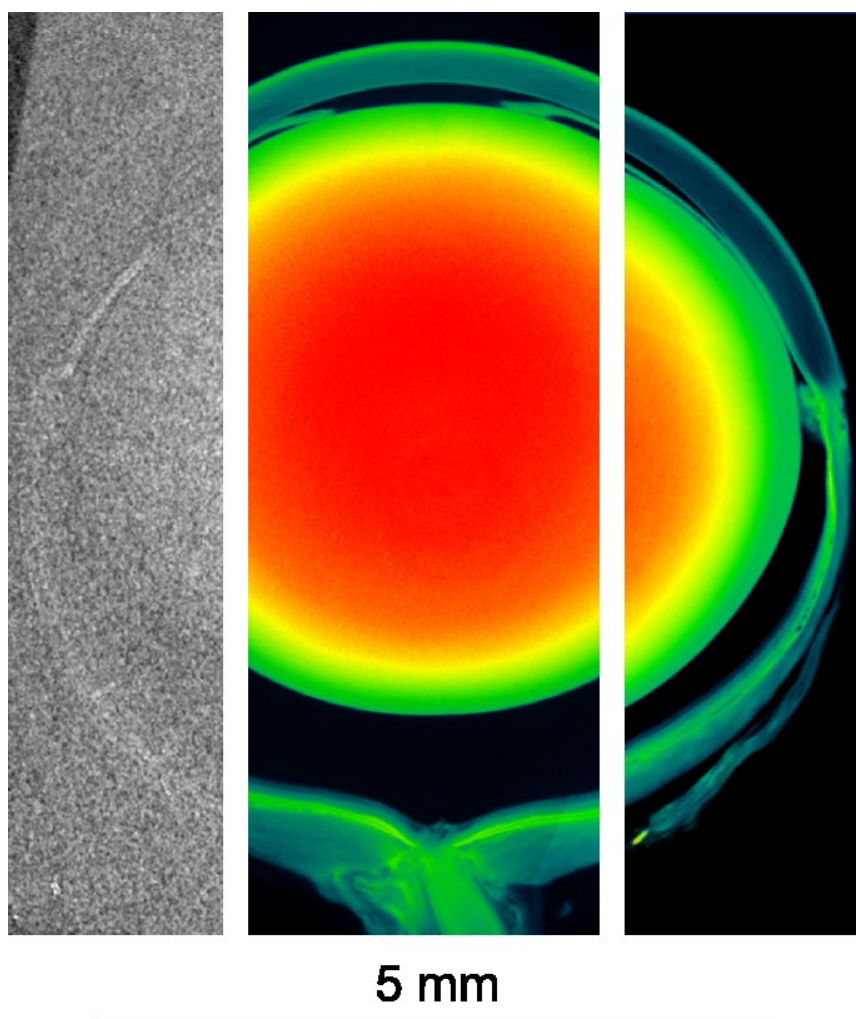
**Figure 18.** Typical μCT images from the unstained control rat eye (2D cross-section, left), I2E stained control eye and I2E stained dystrophic eye (thick 3D slices, center and right respectively). As it can be seen from the leftmost image, it is difficult to distinguish even the major structures of the eye and the small details in the retina are impossible to see at all. In the I2E stained eyes, wide variety of structures are visible. Only the vitreous humour is as dense as the surrounding I2E solution, but especially the lenses seemed to absorb a lot of $I_2$. The eyes are positioned so that the nerve bundles are pointing downward and the corneas are pointing upward. The spatial resolution in the μCT images is approximately 3 μm.

Structural dissimilarities between the dystrophic and control retinas were obvious, as the healthy retinas had much finer and ordered structures. In the control eyes, right next to the choroid, a thin but intense band was observed. This band was followed by a thicker band, after which the rest of the retina faded towards the lens by one lighter step of tone (figure 19). Thus, if the separating layer between the two most intense layers was counted, totally five different retinal layers were observed in the healthy eyes, excluding the choroid and rest of the layers beneath it. It was thought that the most intensive layers contained much of the different pigment molecules, as these polyunsaturated structures will become halogenated by the $I_2$ (figure 8). According the general anatomy of the retinas, this is highly likely as the photosensitive parts of the photoreceptor cells and the retinal

pigment epithelium (RPE) lie close to the choroid (Lens et al., 1999). In the dystrophic eyes, the retinal layers were clearly smeared and the sharp interfaces disappeared. Only somewhat even intensity gradient were seen fading towards the vitreous humour. Clearly, the inability of the RPE to phagocyte and reform the photoreceptor cells disturbed the fine organization of the retina. All these marks were repeatedly seen in all of the imaged eyes. By these qualitative observations it was concluded that the I2E staining was suitable for at least distinguishing structural dissimilarities between the healthy and dystrophic rat eyes.
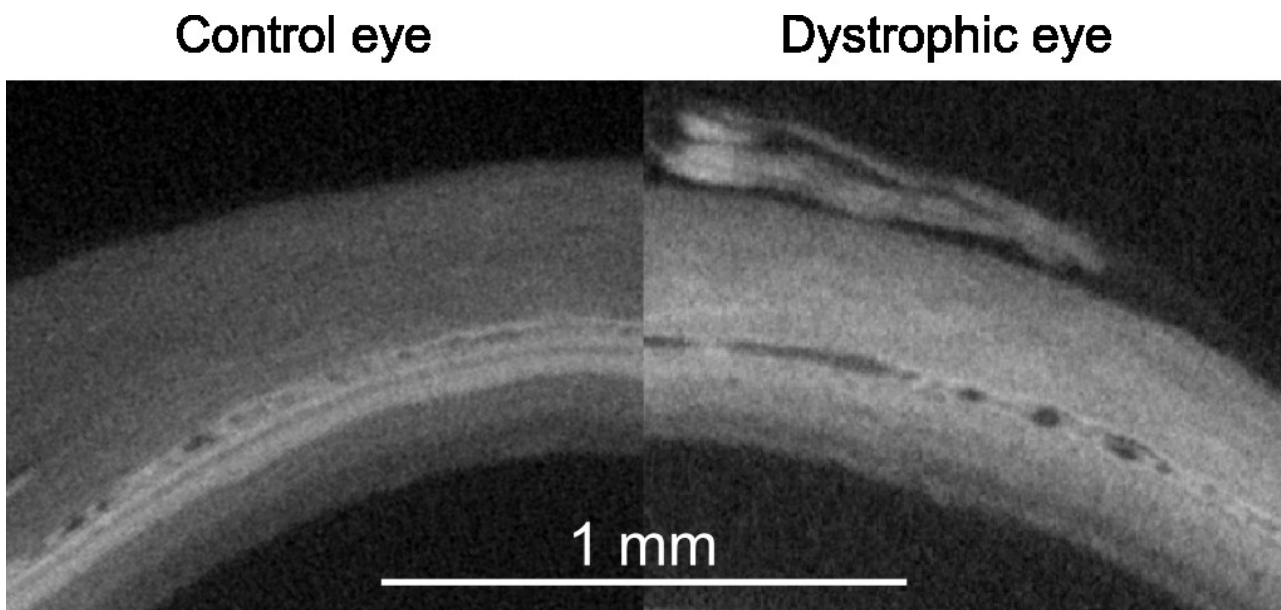


**Figure 19.** Close up images from one of the I2E stained control eye and dystrophic eye stained with the same method. The bottoms of the eyes point upward and the corneas are beneath the figure out of the FOV. By qualitatively examining the eyes it can be quickly seen that the fine structures of the dystrophic retina were smeared. In the control eye, right after the choroid, one thinner and one thicker intensive layers of concentrated $I_2$ can be seen. After these two layers, two somewhat equally thick layers can also be seen, from which the closer one to the vitreous humour was slightly dimmer. In the dystrophic retina, instead of these clearly distinct layers, an intensity gradient was seen fading towards the vitreous humour. The spatial resolution in the μCT images is approximately 3 μm.

## 5.3. Distinctiveness of subcellular structures of ASC
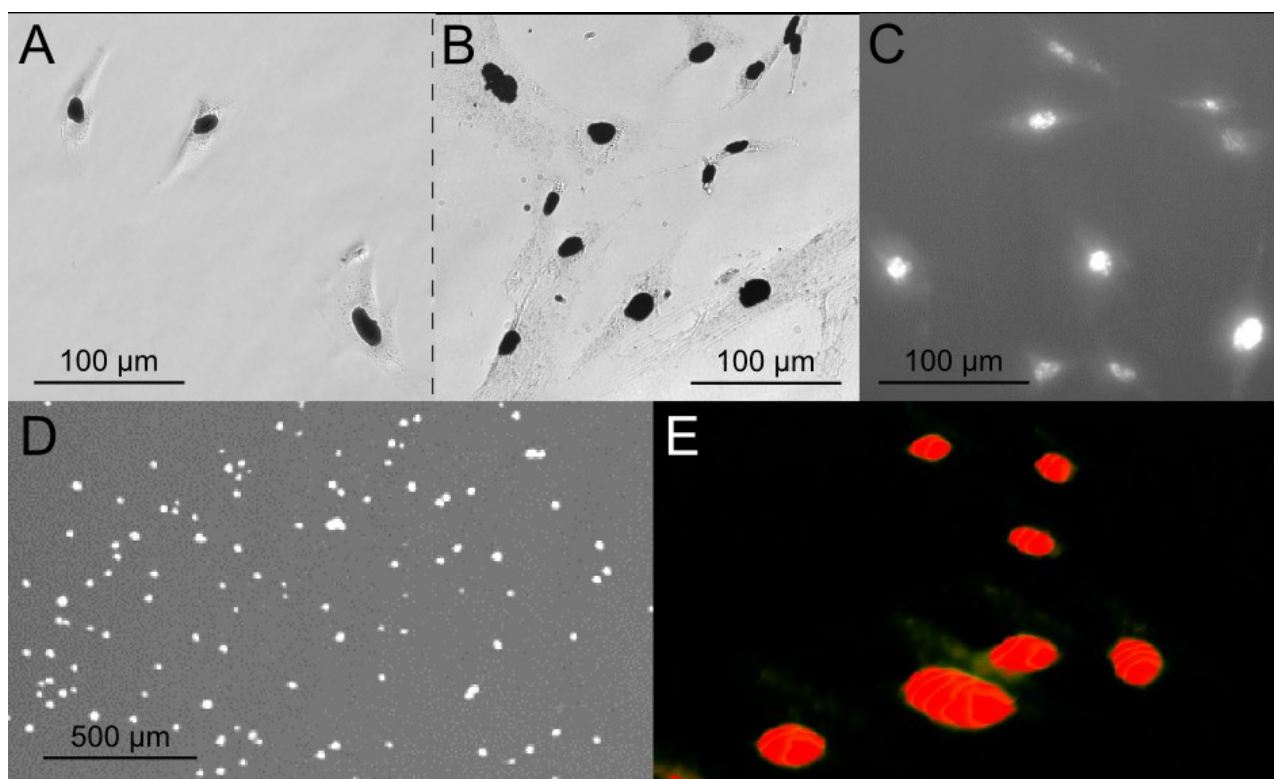
The formed Ag colloids in the ASC cells were clear, intense and localized like excepted (figure 20 and 21). Especially, the lamin-specific signals were sharp, extremely intensive and localized in the shape of the assumed nuclei (figure 21). The β-actin specific signals were comprehensively distributed around the cells, usually excluding the round shapes found in the

middle of the cells (figure 20). These empty holes in the cells were likely nuclei, which lacked the cytoplasmic actin structures. However, while observing the anti-β-acting stained cells with the light microscope, weak Ag signals still arose from the supposed areas of the nuclei in every cell. These weaker signals originated possibly from the actin structures lying beneath and above the nuclei, superimposing the place of it in the 2D examinations. Some of the anti-β-acting stained cells had even relatively intense Ag signals all around the cytoplasm, which is discussed better later.
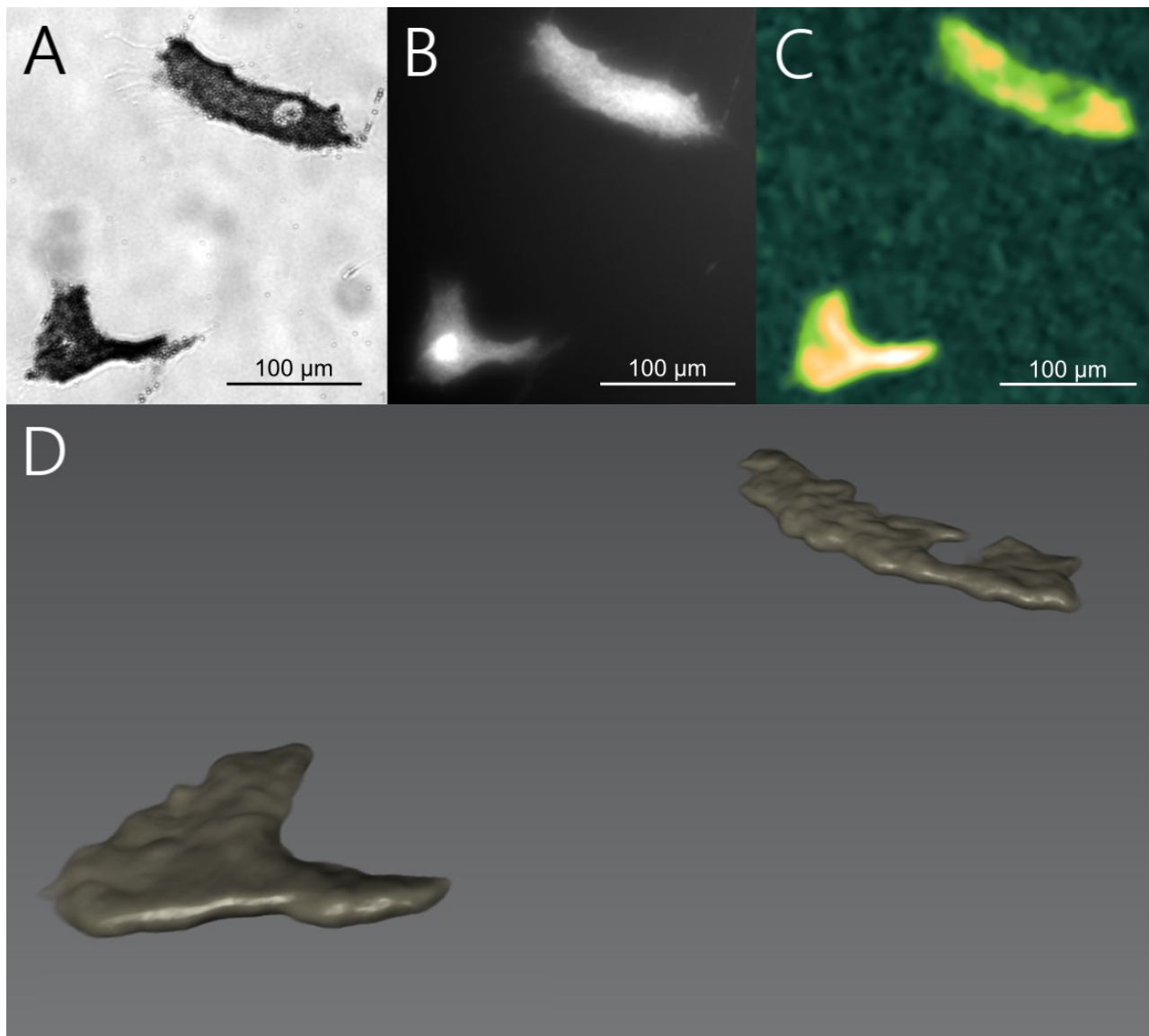


**Figure 20.** The distribution of the anti-β-actin antibody guided Ag colloids in the ASC, imaged by the light microscope (A) and µCT (C and D). The same cells were also imaged with the fluorescence microscope (B) for seeing the co-distribution of the fluorescence labeled phalloidin molecules and the antibody signals. Cells were also 3D rendered with the space fill mode, so that the lower signals under the used threshold level were excluded (D). The scale bar is not provided in D, because of the perspective distortion. Notice the hole in the upper-right cell in D, caused by the spacious nucleus. Simultaneously, no marks of the nucleus are seen in the lower-left cell, which was not punctured in the used 3D rendering (D), but has clearly a not so intense spot approximately in the middle of the cell in the light microscope image (A). The spatial resolution in the µCT images is approximately 1 µm.

**Figure 21.** The distribution of the anti-lamin antibody guided Ag colloids in the ASC, imaged by the light microscope (A and B) and μCT (D and E). The same cells were also imaged with the fluorescence microscope (C) for seeing the co-distribution of the DAPI fluorescence labels with the antibody signals. μCT data shows an overview how the Ag signals were distributed along the surface of the well bottom (lighter tone means higher absorbance, D). The same cells in the close-up and with the different color code (warmer and more opaque colors corresponds to higher absorbance, E). The scale bar is not provided in the 3D rendering image, because of the perspective distortion. The difference in A and B images is that the first cells are fixated by the 4% formaldehyde in PBS, and the B cells with the Davidson's fixative. No remarkable morphological differences can be seen due to different fixation methods. The spatial resolution in the μCT images is approximately 1 μm

When the cells were imaged by μCT, the X-ray absorption signals matched well with the optical signals (figures 20 and 21). In the anti-β-acting stained cells, when the μCT data was examined in 3D, and when the threshold was adjusted to exclude even the strongest background signals from the reconstruction, holes were seen in some of the cells which had the weakest optical Ag signals arising around the possible nuclei (figure 20). On the other hand, with the same threshold adjustment some of the cells did not show any marks of the nuclei. The same more even Ag distribution were also seen in the light microscope examinations. The reason for these differences that some of the cells had clearer nuclear cavities and some of them not, remains unknown. The cells without the clear signal cavity have been hypothesized to be in mitotic phase, where the nucleus breaks down and the actin filaments may spread around the cell (Hiroshi et al., 2005). The possible effects of the cell cycle dynamics on the nuclear morphology were much easier to recognize in the anti-lamin stained cells (figure 21) where the inverse signal distributions were easier to follow

when compared to the anti-β-actin stained cells having more comprehensive Ag distributions. For example, in the figure 21 D, a few close nuclei can be seen, which were possibly in the late phases of the mitosis in the resolving daughter cells.

The parallel fluorescence signals were somewhat similarly distributed with their Ag co-labels, but it is important to remember that the Ag labeled epitopes and the binding sites for the fluorescence labels were not the same. Still, it is worth of discussing about the observed distribution dissimilarities between the antibody and fluorescence co-labels. The co-distribution was clearest in the anti-lamin stained cells, in which the DAPI stain was grainy and weak only approximately in the half of the cells (figure 21 C). These differences between the cells were unknown for sure, but the grainy, even weak DAPI signal was thought to relate to the natural chromatin dynamics and distribution variations in the cell cycle. Thus, the varying DAPI signal intensity might not only report about the packing state of the chromatin, but also reflect the overall localization of the ASC chromosomes in the nuclei, as the proximity of the Ag colloids can block the excitation and emission photons during the fluorescence imaging. The physical mechanism for this phenomenon might be due to absorption and scattering of the photons, as it can be seen in the images 20 A and 21 A and B; the Ag colloids are darkish. Thus, by looking the overall distributions of the darkish Ag colloids and the fluorescent DAPI, it was considered that the lamin-Ag signals lied inside the nuclei. Because of the limited resolving accuracy of the µCT imaging, no remarkable signs were seen about the hollowness of the nuclei.

The co-localization of the phalloidin fluorophores and the anti-β-actin Ag signals was not as clear (figure 20) as it was the case with the anti-lamin and DAPI labeled cells (figure 21). Actually, the phalloidin signal was highly intensive in the supposed locations of the nuclei, while the signal intensity was only moderate in the other parts of the cells. There is a reasonable explanation for these distribution differences. Like discussed earlier, the fluorescence signal could be damped because of the presence of the colloidal Ag. The fluorescence signals might be more intensive around the nuclei, because there are less Ag colloids nearby, absorbing and scattering the traveling fluorescence photons. Thus, the phalloidin might actually be distributed evenly inside the cells, excluding the nuclei, but strong signals can only be seen around the nuclei where the fluorescence imaging is not so strongly disturbed by the Ag colloids. At least in the parallel control samples, which

were not stained with the Ag colloids, the fluorescence signal arising from the phalloidin was equally distributed around the cells and no marks of nuclei were seen.

No remarkable morphological differences were seen, whether the cells were fixed by the 4% formaldehyde in PBS solution or with Davidson's fixative, tried with the lamin-stained ASC (figure 21). The ready-to-use horse serum blocking solution and the 4% w/v BSA in PBS did not either have different effects on the final contrasting results like expected.

# 6. Conclusions

As a final summary, the three tested background contrasting methods were successfully optimized for examining different kinds of histological samples. All of the trialed background stains were found to greatly enhance the soft tissue visibility during µCT imaging. Furthermore, the PTA-endogenous-phosphate-precipitation issue was taken into account and all three tested background stains were successfully applied on the relatively large adult zebra fish samples. Thus, the earlier work with these contrasting agents were advanced further (Metscher, 2009; Pauwels et al., 2013). It was further shown for the very first time that the I2E enhanced µCT imaging is suitable for examining the fine structural dissimilarities between the healthy and dystrophic RCS rat retinas. Finally, specific antibody labeling gave reliable results which further encourages to apply the X-ray tube radiation based µCT devices for studying even subcellular antigen distributions in biological samples.

I2E staining was the quickest and most straightforward of the all background stains, and gave comprehensive insight into the general anatomy of the adult zebra fish. It was also considered to be the safest method for preserving the fragile morphology of the rat retinas, as it includes similar increasing alcohol dehydration series as used in the conventional histology. By comparing qualitatively the control and RCS dystrophy eyes, it become immediately clear that the two types of eyes had fine structural dissimilarities. It was considered that I2E stains the polyunsaturated pigments found in retinas, and it was found that the control retinas were highly ordered in structure while the fine cellular hierarchy in the dystrophic retinas was severely disturbed. These observations led to the conclusion that the I2E contrasting was suitable method for µCT examinations of the dystrophy pathogenesis in the rat eyes.

The IKI stain was found to be the best choice for preserving fatty tissues in the adult zebra fish samples, while the other background stains possibly dissolved them due to the presence of ethanol. The semi-specificity against fat of IKI stain raised thoughts about its possible future applications. For example, by the IKI stain one could examine obesity by mapping fatty tissues and their amounts, after different, forced feeding habits, induced diseases or medicines are applied on the studied model organisms.

The PTA gave generally as good contrast enhancement as the other stains, but it was the most complicated to apply. After optimization, PTA contrasting was still feasible with the relatively large histological samples of adult zebra fish, even though the contrasting took more time than the other contrasting methods. The possible precipitation artefacts with phosphates were taken into account, which was not considered in the earlier reported contrasting experiments with much smaller chick embryos (Metscher, 2009). The PTA stain might give more distinctive and easier results with the other kinds of samples, but its best feature in the experiment with the zebra fish samples was its capability to preserve the morphology of the stained samples. PTA caused no inward wrinkling of the skin, for example, which was seen in the I2E and IKI stains.

Specific antibody guided Ag labels worked as intended. By examining the cellular morphology and Ag distribution patterns after the labels, it was quite clear that the Ag signals localized as they were supposed to. Anti-β-actin signals were comprehensively distributed along the cytoplasm and some of the cells had clear nucleus-like signal cavities. Some of the cells did not have these empty cavities, which was possibly due to natural cell cycle dynamics as some of the nuclei were broken down for mitosis and giving actins more liberty locate in the cells. The co-distribution of the Ag signals and the phalloidin fluorophores were similar in the anti-β-actin labeled cells, excluding the high intensity fluorescence signals arising from the mentioned Ag signal cavities. This was probably due to the fluorescence damping by the Ag colloids; the Ag free cavities did not absorb and/or scatter the emission and excitation photons used in the fluorescence examinations. In the anti-lamin stained cells the Ag signals were intensive and extremely sharply localized in the nucleus-like structures; Ag distributions were like inverse version of the anti-β-actin labeled cells. The parallel DAPI signals were well superimposed on the Ag signals, but some nuclei were seen grainy, other nuclei actually quite dim. It was concluded that the same effects of the cell cycle dynamics, varying chromatin localization and the light absorbing and scattering Ag colloids resulted these DAPI intensity variations. Thus, both of the used contrasting labels gave reliable signals which were possible to examine with the used μCT device.

# 7. References

Appel AA, Anastasio MA, Larson JC, Brey EM. Imaging challenges in biomaterials and tissue engineering. Biomaterials, 2013;34:6615–6630.

Bancroft JD and Gamble M. Theory and Practice of Histological Techniques. Elsevier, China, 2008.

Beutel J, Kundel HL, Van Metter RL. Handbook of medical imaging. Volume I: Physics and psycophyics. SPIE Press, Washington, 2000.

Bilderback DH, Elleaume P, Weckert E. Review of third and next generation synchrotron light sources. Journal of physics: atomic, molecular and optical physics, 2005;38:773-797.

Boone JM, Seibert JA, Fewell TR, Jennings RJ. Simulation of X-ray Spectra. Siemens, https://w9.siemens.com/cms/oemproducts/home/x-raytoolbox/spektrum/pages/default.aspx (March 10, 2014).

Brunkea O, Brockdorfb K, Drewsc S, Müllerc B, Donathd T, Herzend J, Beckmannd F. Comparison between X-ray tube based and synchrotron radiation based μCT. SPIE proceedings, 2008;70780U.

Buchwalow IB and Böcker W. Immunohistochemistry: Basics and Methods: Basics and Methods. Springer, New York, 2010.

Cheng KC, Xin X, Clark DP, Riviere PL. Whole-animal imaging, gene function, and the zebrafish phenome project. Current opinion in genetics & development, 2011;21:620-629.

Chien CC, Tseng PY, Chen HH, Hua TE, Chen ST, Chen YY, Leng WH, Wang CH, Hwu Y, Yin GC, Liang KS, Chen FR, Chu YS, Yeh HI, Yang YC, Yang CS, Zhang GL, Je JH, Margaritondo G. Imaging cells and sub-cellular structures with ultrahigh resolution full-field. Biotechnology Advances, 2013;31:375-386.

Chu X, Xiang ZF, Fu X, Wang SF, Shen GL, Yu RQ. Silver-enhanced colloidal gold metalloimmunoassay for Schistosoma japonicum antibody detection. Journal of immunological methods, 2005;301:77-88.

Cox PG and Jeffery N. Reviewing the morphology of the jaw-closing musculature in squirrels, rats, and guinea pigs with contrast-enhanced microCT. The anatomical record, 2011;294:915-928.

Daneke N and Schanklies B. X-ray Inspection: Evolution from Microfocus to Nanofocus. Solid state technology - insights for electronics manufacturing, 2004, http://electroiq.com/blog/2003/12/x-ray-inspection-evolution-from-microfocus-to-nanofocus/ (March 10, 2014).

Danila D, Johnson E, Kee P. CT imaging of myocardial scars with collagen-targeting gold nanoparticles. Nanomedicine: nanotechnology, biology, and medicine, 2013;9:1067-1076.

Dorsey SM, Lin-Gibson S, Simon SG, Jr. X-ray microcomputed tomography for the measurement of cell adhesion and proliferation in polymer scaffolds. Biomaterials, 2009;30:2967-2974.

Eck W, Nicholson AI, Zentgraf H, Semmler W, Bartling S. Anti-CD4-targeted Gold Nanoparticles Induce Specific Contrast Enhancement of Peripheral Lymph Nodes in X-ray Computed Tomography of Live Mice. NANO Letters, 2010;10:2318-2322.

Eijk CWE. Inorganic scintillators in medical imaging detectors. Nuclear instruments and methods in physics research, 2003;509:17-25.

EnzMet™ for General Research Applications. Nanoprobes, catalog number 6010, manual 2014.

Feynman RP, Leighton RB, Sands ML. The Feynman lectures on physics. Volume III - quantum mechanics. Original third printing 1966. The new millennium edition, Basic books, New York, 2011.

Frey PA and Hegeman AD. Enzymatic Reaction Mechanisms. Oxford university press, New York, 2007.

Gao D, Pogany A, Stevenson AW, Wikins SW. Phase-contrast radiography. Radiographics, 1998;18:1257-1267.

Görlich EA. Polish synchrotron light source - Status of the project. Radiation physics and chemistry, 2009;78:140-141.

Hainfeld JF, O'connor MJ, Dilmanian FA, Slatkin DN, Adams DJ, Ssmilowitz HM. Micro-CT enables microlocalisation and quantification of Her2-targeted gold nanoparticles within tumour regions. The British journal of radiology, 2011;84:526-533.

Hamilton RJ. Lipid Analysis of Oils and Fats. Springer, New York, 1997.

Hann CR, Bentley MD, Vercnocke A, Ritman EL, Fautsch MP. Imaging the aqueous humor outflow pathway in human eyes by three-dimensional micro-computed tomography (3D micro-CT). Experimental eye research, 2011;92:104-111.

Hiroshi Y, Katsuhiro K, Hiroyuki K, Kayoko S, Shin-ichiro K, Shin-ichiro E. Localization of actin filaments on mitotic apparatus in tobacco BY-2 cells. Planta, 2005;222:118-129.

Holdsworth DW and Thornton MM. Micro-CT in small animal and specimen imaging. Trends in biotechnology, 2002;20:4-39.

Jeffery NS, Stephenson RS, Gallagher JA, Jarvis JC, Cox PG. Micro-computed tomography with iodine staining resolves the arrangement of muscle fibres. Journal of biomechanics, 2011;44:189-192.

Joshi NS, Bansal PN, Stewart RC, Snyder BD, Grinstaff MW. Effect of contrast agent charge on visualization of articular cartilage using computed tomography: exploiting electrostatic interactions for improved sensitivity. JACS Communications, 2009;131:13234-13235.

Kalender W. Photon, proton, and neutron interaction data for body tissues. ICRU report, 1992;46.

Kazakia GJ, Burghardt AJ, Cheung S, Majumdar S. Assessment of bone tissue mineralization by conventional x-ray microcomputed tomography - Comparison with synchrotron radiation microcomputed tomography and ash measurements. Medical physics, 2008;35:3170-3179.

Kneip S, McGuffey C, Martins JL, Martins SF, Bellei C, Chvykov V, Dollar F, Fonse R, Huntington C, Kalintchenko G, Maksimchuk A, Mangles SPD, Matsuoka T, Nagel SR, Palmer CAJ, Schreiber J, Phuoc KT, Thomas AGR, Yanovsky V, Silva LO, Krushelnick K, Najmudin Z. Bright spatially coherent synchrotron X-rays from a table-top source. Nature physics, 2010;6:980-983.

Kondo H, Ikeda K, Miyazaki N. The mechanism of Bodian's silver staining: effect of copper ion on silver impregnation. Journal of neuroscience methods, 1996;68:275-280.

Lens L, Nemeth SC, Ledford JK. Ocular anatomy and physiology. SLACK Incorporated, New Jersey, 1999.

Marsich L, Bonifacio A, Mandal S, Krol S, Beleites C, Sergo V. Poly-L-lysine-coated silver nanoparticles as positively charged substrates for surface-enhanced Raman scattering. Langmuir, 2012;28: 13166–13171.

Metscher BD and Muller GB. MicroCT for Molecular Imaging: Quantitative Visualization of Complete Three-Dimensional Distributions of Gene Products in Embryonic Limbs. Developmental dynamics, 2011;240:2301-2308.

Metscher BD. MicroCT for Developmental Biology - a versatile tool for high-contrast 3D imaging at histological resolution. Developmental dynamics, 2009;238:632-640.

Nelson DM, Mab Z, Fujimoto KL, Hashizume R, Wagner WR. Intra-myocardial biomaterial injection therapy in the treatment of heart failure - materials outcomes challenges. Acta biomaterialia, 2011;7:1-15.

Pauwels E, Loo VD, Cornillie P, Brabant L, LV Hoorebeke. An exploratory study of contrast agents for soft tissue visualization by means of high resolution X-ray computed tomography imaging. Journal of microscopy, 2013;250:21-31.

Ritman EL. Molecular Imaging in Small Animals - Roles for Micro-CT. Journal of Cellular Biochemistry Supplement, 2002;39:116-124.

Robyt JF. Essentials of Carbohydrate Chemistry. Springer, New York, 1998.

Ruan MZC, Dawson B, Jiang M, Gannon F, Heggeness M, Lee BHL. Quantitative Imaging of Murine Osteoarthritic Cartilage by Phase-Contrast Micro-Computed Tomography. Arthritis & rheumatism, 2013;65:388-396.

Schambach SJ, Bag S, Schilling L, Groden C, Brockmann MA. Application of micro-CT in small animal imaging. Methods, 2010;50:2-13.

Seibert JA and Boone JM. X-Ray Imaging Physics for Nuclear Medicine part 2 - X-ray interactions and image formation. Journal of nuclear medicine technology, 2005;33:3-18.

Silver Enhancer Kit. Sigma-Aldrich, catalog number SE100, manual 2014.

Stampanoni M, Borchert G, Abela R, Rüegsegger P. Bragg magnifier: A detector for submicrometer x-ray computer tomography. Journal of applied physics, 2002;92: 7630- 7635.

Stephenson RS, Boyett MR, Hart G, Nikolaidou T, Cai X, Corno AF, Alphonso A, Jeffery A, Jarvis JC. Contrast Enhanced Micro-Computed Tomography resolves the 3dimensional morphology of the cardiac conduction system in mammalian hearts. Plosone, 2012;7:1-11.

Thimm BW, Hofmann S, Schneider P, Carretta R,Muller R. Imaging of Cellular Spread on a Three-Dimensional scaffold by means of a novel cell-labeling technique for high-resolution computed tomography. Tissue engineering, 2012;18:167-175.

Ven L and Wester P. Histology and Histopathology Atlas of the Zebrafish. V2.01, http://zfishtoxpat.comoj.com/tesloc.html (April 10, 2014).

Voronov RS, VanGordon SB, Shambaugh RL, Papavassiliou DV, Sikavitsas DI. 3D Tissue-Engineered Construct Analysis via Conventional High-resolution Microcomputed Tomography Without X-ray Contrast. Tissue engineering, 2013;19:327-335.

Watlinga CP, Lagob N, Benmerahc S, FitzGeraldd JJ, Tartec E, McMahonb S, Lacoure SP, Camerona RE. Novel use of X-ray micro computed tomography to image rat sciatic nerve and integration into scaffold. Journal of neuroscience methods, 2010;188:39-44.

Webb S. The physics of medical imaging. Medical science series. CRC Press, Florida, 1988.

Yamanea S, Iwasakia N, Majimaa T, Funakoshia T, Masukoa T, Haradac K, Minamia A, Mondeb K, Nishimurab SI. Feasibility of chitosan-based hyaluronic acid hybrid biomaterial for a novel scaffold in cartilage tissue engineering. Biomaterials, 2005;26:611-619.

Yue S, Lee PD, Poologasundarampillai G, Yao Z, Rockett P, Devlin AH, Mitchell CA, Konerding MA, Jones JR. Synchrotron X-ray microtomography for assessment of bone tissue scaffolds. Journal of materials science, 2010;21:847-853.

Zehbe R, Goebbels J, Ibold Y, Gross U, Schubert H. Three-dimensional visualization of in vitro cultivated chondrocytes inside porous gelatine scaffolds: A tomographic approach. Acta biomaterialia, 2010;6:2097-2107.

Zhu Z, Tain R, Rhodes C. A study of the decomposition behavior of 12-tungstophosphate heterpolyacid in solution. Canadian journal of chemistry, 2003;81:1044-1050.